

ACOUSTIC EMISSION FROM THE CRYSTALLIZATION
OF POTASSIUM BROMIDE DOPED WITH LEAD

by

ADRIAN P. COOK

B.Sc., The University of Nottingham, U.K., 1989

A THESIS SUBMITTED IN PARTIAL FULFILMENT OF
THE REQUIREMENTS FOR THE DEGREE OF
MASTER OF SCIENCE

in

THE FACULTY OF GRADUATE STUDIES
DEPARTMENT OF CHEMISTRY

We accept this thesis as conforming
to the required standard



THE UNIVERSITY OF BRITISH COLUMBIA

JANUARY 1993

© Adrian Cook, 1993

In presenting this thesis in partial fulfilment of the requirements for an advanced degree at the University of British Columbia, I agree that the Library shall make it freely available for reference and study. I further agree that permission for extensive copying of this thesis for scholarly purposes may be granted by the head of my department or by his or her representatives. It is understood that copying or publication of this thesis for financial gain shall not be allowed without my written permission.

(Signature)



Department of Chemistry

The University of British Columbia
Vancouver, Canada

Date 16 February 1993

Abstract

Simultaneous optical and acoustic information was used to elucidate the mechanism that causes acoustic emission (AE) during growth of potassium bromide (KBr) crystals. The generation mechanism postulated here is one of *inter-crystal interaction*. AE was used to monitor the growth of different crystal structures of KBr grown with varying degrees of lead (Pb) dopant (0-32000 ppm). Digital images were collected simultaneously at magnifications up to x75. Integrated AE profiles and image whitening curves were calculated. Best agreement between these was found for the crystal growth of the dendritic form of KBr (4080-8120 ppm Pb dopant), and the doped forms of 12210 ppm Pb and above. The dendritic form of KBr observed between 4080 and 8120 ppm Pb consisted of finger-like needles that grew outward from the crystallizing solution. Scanning electron microscopy showed these fingers to consist of contiguous chains of tiny (< 25 μm dia.) octahedra. This microscopic structure provided many potential sources of emission. The total AE observed per gram of crystals produced during the growth of the different KBr morphologies was found to vary in a reproducible manner over 60 experiments. The dendritic form of KBr exhibited 10 times the acoustic emission per gram of crystals produced compared with the undoped (cubic) form. The mass of crystals grown for individual experiments was 0.004-0.212 g. AE was able to reliably follow the growth of these very small masses of crystals whose morphologies consisted of clusters of crystals in intimate contact. A confirmatory mechanistic study was carried out using ammonium chloride (NH_4Cl) which is known to produce classic dendritic growth. In contrast to the clusters of tiny microcrystals observed for the dendritic form of KBr, one would not expect the growth of the single crystal branches of NH_4Cl to exhibit acoustic emission, as there is no means to generate AE by the *inter-crystal interaction* mechanism. Single branch fracture is possible but rare. Experimental results showed very limited emission from NH_4Cl , and thus supported the

hypothesis of *inter-crystal interaction*. Primary nucleation could not be detected acoustically. The end of crystal growth was acoustically determinable. The AE associated with the growth of the dendritic form of KBr finished abruptly when the maximum image whiteness was reached. The acoustic waveforms detected during the growth of the KBr morphologies were compared with artificially produced signals of bulk fracture and crystal impact. Acoustic waveform analysis showed these classes of signals to be distinguishable.

CONTENTS

Abstract	ii
List of Tables	vii
List of Figures	viii
I Introduction	
1.1 Acoustic Methods in Chemistry	1
1.2 Acoustic Emission	1
1.2.1 Acoustic Emission Experimental Techniques	2
1.3 Acoustic Emission Data Analysis	4
1.3.1 Acoustic Waveform Analysis	4
1.3.2 Principal Components Analysis	6
1.4 Crystallization Processes	7
1.4.1 Nucleation	7
1.4.2 Growth	8
1.4.3 Growth Forms	8
1.5 Effect of Impurities on Crystal Growth	10
1.6 Crystal Growth Monitoring	11
1.7 Acoustics and Crystallization	12
1.8 Crystal Growth of KBr	14
1.8.1 Effect of Lead Impurity	16
1.9 Purpose of the Present Work	18

II Experimental

2.1	Reagents	19
	2.1.2 Solution Preparation	19
2.2	Apparatus	20
	2.2.1 Image Acquisition Apparatus	20
	2.2.2 Software Development for Image Acquisition	22
	2.2.3 Apparatus for Acoustic Emission Detection	22
	2.2.4 Modes of Acoustic Acquisition	23
	2.2.5 Acoustic Emission Integration	23
	2.2.6 Individual Acoustic Signal Detection and Collection	24
	2.2.7 Ex-situ Analysis Methods	27
2.3	Experimental Procedure	28
	2.3.1 General Procedure for KBr Morphological Studies	28
	2.3.2 Preliminary Experiments	29
	2.3.3 Complete Morphological Study	29
	2.3.3.1 Acoustic Integration and Optical Imaging	29
	2.3.3.2 Capture of Acoustic Waveforms Arising During Crystal Growth	32
	2.3.4 Artificially Produced Acoustic Signals from Crystallization Processes	32
	2.3.5 Primary Nucleation Study	32
	2.3.6 Dendritic Growth Study	34
2.4	Data Analysis Methods	34
	2.4.1 Integrated Acoustic Emission and Image Whitening Analysis	34
	2.4.2 Acoustic Waveform Analysis	35

III Results and Discussion	
3.1 Findings of Preliminary Morphological Study of KBr	38
3.1.1 Trends in Integrated Acoustic Emission	38
3.2 Comprehensive Morphological Study of KBr	40
3.2.1 Crystallization Sequences at a Magnification of x20	40
3.2.2 Studies at Magnification x75	48
3.2.3 EDX and XRD Analysis of Needles	48
3.2.4 Trends in Integrated Acoustic Emission	53
3.3 Source of the Acoustic Emission	55
3.3.1 Comparison of the Rate of Acoustic Emission and Rate of Crystallization	55
3.3.2 Integrated Acoustic Emission and Image Whitening Rise Times	58
3.3.3 Dimensionality of the Dendritic Growth Form	61
3.3.4 Fracture Related Damage at High Dopant Levels	65
3.4 Characterization of Crystallization Processes by Acoustic Waveform Analysis	65
3.4.1 Generation of Different Signal Classes	65
3.4.2 Signal Intensities	66
3.4.3 Signal Class Separation by PCA	70
3.5 Classic Dendritic Growth	78
3.6 Primary Nucleation	80
IV Conclusions	81
V Further Work	83
Literature Cited	85

LIST OF TABLES

Table I:	Descriptors used to mathematically characterize each acoustic signal.	5
Table II:	Average values of weight and atomic percentages of K, Pb, Br determined by Energy Dispersive X-ray Analysis for needle crystals shown in fig. 15a.	49
Table III:	Average values of weight and atomic percentages of K, Pb, Br determined by Energy Dispersive X-ray Analysis in the octahedral matrix shown in fig. 15a.	49
Table IV:	Powder X-ray diffraction peak positions for K_2PbBr_4 and KBr.	51
Table V:	Descriptors that showed the highest resolution for the 6 different classes of crystallization signals.	71
Table VI:	Descriptors that showed the highest resolution for the pairwise separation of artificial signals of bulk fracture and crystal impact, from the cubic (undoped) form of KBr, and the dendritic (doped) form of KBr.	73

LIST OF FIGURES

Figure 1.	Growth of crystal faces. Adapted from reference [60].	9
Figure 2.	Unit cell of potassium bromide.	14
Figure 3.	Classic dendritic growth.	15
Figure 4.	Schematic representation of the change in habit of KBr from cubic to octahedral on the addition of lead impurity. Adapted from reference [61].	17
Figure 5.	Apparatus schematic.	25
Figure 6.	(a) Transducer's frequency response curve, (b) Background frequency spectrum of blank.	26
Figure 7.	Arrangement used for crystal growth experiments.	30
Figure 8.	Typical image of cubic KBr crystals on the surface of the transducer. Image viewed through a continuously focusable microscope with a magnification of x20.	31
Figure 9.	Experimental arrangement for KBr whisker formation.	33
Figure 10.	Data analysis strategy for acoustic waveforms collected during crystallization processes.	37
Figure 11.	Dendritic form of KBr crystals observed with 4923 ppm Pb dopant. Growth of fingers on the transducer surface.	38
Figure 12.	Variation of total acoustic emission per gram of KBr crystals grown during preliminary study. Crystal morphology influenced by Pb doping.	39
Figure 13.	Scanning electron micrographs of (a) cubic KBr at 0 ppm Pb dopant, and (b) cubic to octahedral change of KBr at 1990 ppm Pb dopant.	43
Figure 14.	Scanning electron micrographs of (a) central islands of KBr observed in droplet at 4080 ppm Pb dopant, showing the clustering of the octahedra, and (b) dendritic fingers of KBr with 6070 ppm Pb dopant.	44

Figure 15.	Scanning electron micrographs of (a) K_2PbBr_4 needles in an octahedral matrix of KBr, observed at 24840 ppm Pb dopant, and (b) enlargement of the central portion of fig. 15a, showing the interpenetration of a needle with the octahedral matrix.	45
Figure 16.	Integrated acoustic emission and image whitening curves with time, for the growth of KBr crystals viewed at a x20 magnification with varying amounts of lead dopant, (a) 0 ppm Pb, (b) 1990 ppm Pb, (c) 4080 ppm Pb, and (d) 22060 ppm Pb.	46
Figure 17.	Integrated acoustic emission and image whitening curves with time, for the growth of the dendritic form of KBr crystals with 8120 ppm Pb. Two different magnifications shown, (a) x20, and (b) x75.	47
Figure 18.	Powder X-ray diffraction patterns for (a) needle crystals collected during the growth of KBr crystals from a solution doped with 29790 ppm Pb, and (b) analytical grade KBr.	52
Figure 19.	Total acoustic emission per gram of KBr crystals grown with varying amounts of lead dopant. 3 experimental series are shown.	54
Figure 20.	Integrated acoustic emission profiles observed during the growth of KBr crystals with varying degrees of lead dopant.	59
Figure 21.	Comparison of acoustic integration and image whitening rise times as the KBr crystal morphology is changed by increasing the lead dopant.	60
Figure 22.	Total acoustic emission per gram of crystals produced during the growth of 5 replicate samples of KBr doped with 8120 ppm Pb.	62
Figure 23.	Effect of vapour pressure on the total acoustic emission per gram of crystals produced during the growth of the dendritic form of KBr with 8120 ppm Pb. Numbers 1-5 refer to replicates of fig. 22.	64

Figure 24.	Typical acoustic signals and associated power spectra for KBr crystals grown with (a) 0 ppm, (b) 7620 ppm and (c) 24920 ppm Pb dopant, (d) bulk fracture of fingers of KBr grown with 7620 ppm Pb dopant, and (e) impact of KBr crystals on the transducer surface.	68
Figure 25.	Average power spectra for acoustic signals collected during the growth of KBr crystals with (a) 0 ppm, (b) 7620 ppm, (c) 24920 ppm Pb dopant, and artificially produced signals of (d) bulk KBr dendrite fracture, (e) KBr crystal impacts on the transducer.	69
Figure 26.	Principal components analysis showing the separation of different crystallization processes. Only 18 of 32 descriptors were used (see table V).	72
Figure 27.	Principal components analysis showing the separation of acoustic signals that occurred during crystal growth from artificially generated signals mimicking secondary nucleation processes.	75
Figure 28.	Principal components analysis of acoustic signals collected from both artificially produced crystallization processes, and actual growth processes of different KBr crystal morphologies.	76
Figure 29.	Principal components analysis of acoustic signals collected with a 2.5 MHz bandwidth during the growth of different KBr crystal morphologies. Only 18 of 32 descriptors were used (see table V).	77
Figure 30.	Integrated acoustic emission profile for the dendritic growth of ammonium chloride, showing the infrequent signals, leading to a stepped plot.	79
Figure 31.	Scanning electron micrographs of (a) dendritic NaCl, (b) granular NaCl. Reproduced from reference [68].	84

ACKNOWLEDGEMENTS

Many thanks are due to all my lab mates both past and present who suffered through this thesis, but particularly to Larry, Oliver, Helen and Kevin. Special thanks go to Heather and Jim for keeping me sane, as well as to my parents for much needed advice.

For tuition and the explanation of many queries concerning scanning electron microscopy thank you to Mary Mager, and similarly to Norman Osborne for XRD tuition. Thanks must also be extended to those at Infracan Inc. (Richmond) for the help with the production of figure 8.

Finally, thanks to my supervisor Adrian Wade, and to the following agencies for my support; the Canadian National Networks of Centres of Excellence, the Institute for Chemical Science and Technology and the National Science and Engineering Research Council of Canada.

"Where the telescope ends, the microscope begins.

Which of the two has the grander view?"

Victor Hugo : Les Misérables III. iii.

I INTRODUCTION

1.1 Acoustic Methods in Chemistry

There are three broad categories of acoustic methods within chemistry. Firstly, an external sound source (ultrasonic) can be used to enhance chemical reactions; this is referred to as sonochemistry [1]. Secondly, external acoustic sources may be used as analytical probes, such as in acoustic microscopy [2], ultrasonic imaging and surface acoustic wave (SAW) devices [3]. Thirdly, one may detect acoustic waves produced within the material which accompany certain chemical and physical changes of the material. Photoacoustic spectroscopy whereby acoustic waves are generated within a sample due to the absorption of optical radiation [4, 5] and Acoustic Emission (AE) fall into this third category. The latter is the method employed in this thesis.

1.2 Acoustic Emission

Acoustic emissions are transient elastic waves resulting from a rapid release of energy within a material [6]. The acoustic emission takes the form of many bursts of high frequency (50kHz-5MHz) acoustic energy. These bursts are generated by the rapid mass motion or physical transformation of large collective groups of atoms. A number of physical processes have been cited as sources of acoustic emission, such as bubble bursting [7, 8], the motion of dislocations [9], propagation of cracks and crystal fracture [9, 10], and rapid volume changes that can occur during phase transitions and polymorphic transformations [11, 12].

1.2.1 Acoustic Emission Experimental Arrangements

Acoustic emission signals can be readily detected using a piezoelectric transducer, which converts the acoustic pressure wave to an electrical impulse. The duration and frequency content of the acoustic wave produced are indicative of the underlying physical mechanism that produced the acoustic burst. Indeed, signals from different physical processes such as crystal fracture and bubble formation have been distinguished based on the acoustic characteristics of their pressure waves [13].

Unfortunately, the original acoustic wave and that detected by the transducer will not be identical. The final signal detected will be modified by its transmission through the reacting medium, and across any container and transducer interfaces. Despite this, sufficient information is retained in the signal to study and sometimes identify the physical mechanism that produced it. In order to ensure good acoustic transmission across the transducer reaction vessel interface an acoustic couplant is used between the reaction vessel and the transducer surface. This couplant is designed to minimize attenuation at the interface and is usually an exceptionally viscous liquid such as petroleum jelly [14]. These problems of attenuation and propagation of the acoustic wave across all the interfaces in a standard experimental arrangement have detracted somewhat from the advantage of AE as a non-invasive, non-destructive analytical technique [15, 16]. One approach to this problem is to remove as many interfaces as possible by conducting experiments directly on the transducer surface, so increasing the experimental reproducibility.

An experimental arrangement for AE monitoring would typically consist of a piezoelectric transducer, an amplifier and a recording device. The recording device chosen depends on the information sought. The simplest recording device is a chart recorder. The direct current (d.c.) output from commercially available acoustic emission

amplifiers provides peak level (signal intensity) information. The chart recorder trace shows the number of acoustic signals (as individual spikes) and the duration of the AE. Event counters, or acoustic power integrators can also be used to follow the kinetics of the process emitting AE by monitoring the d.c. output. A high speed digitizer can be used for individual acoustic signal capture if frequency signatures of the process are required. This is achieved by connecting the digitizer to the alternating current (a.c.) output from the amplifier. Acoustic signals from the process being monitored are distinguished from background noise by selecting a trigger level voltage which is greater than the peak amplitude of the background acoustic signals. Most processes monitored by AE in this laboratory emit in the ultrasonic region ($>20\text{kHz}$), and so a high-pass filter may be used to eliminate any ambient noise in the audible region (3-16kHz).

Many commercially available broad-band or resonant piezoelectric transducers are suitable for the detection of AE. The commonest design consists of a small (approx 1mm^2) piezoelectric crystal of a material such as lead zirconate titanate, protected by a thin metal case (commonly stainless steel). Such sensors have bandwidths within the range 2kHz-4MHz. The frequency response of these transducers is unfortunately not flat over this bandwidth, and substantial variability is often encountered even between the responses of transducers of the same model. This transducer variability, together with the problems associated with the attenuation and propagation of the acoustic wave through the experimental apparatus, means that for comparisons between experiments to be valid the same experimental arrangement and transducer must be used throughout a series of experiments.

1.3 Acoustic Emission Data Analysis

There are two main methods of acoustic emission data analysis. The first simply involves the integration of the d.c. signal with time, enabling the rate and amount of acoustic emission produced to be followed. The second method involves the waveform analysis of the acoustic signals, and is more complex.

1.3.1 Acoustic Waveform Analysis

Typically 1000's of signals may be collected in a single experiment. Computer aided statistical pattern recognition techniques are used to look for differences and similarities in the acoustic signals. In order for the computer to compare the acoustic signals each signal may first be mathematically represented by a number of time domain and frequency domain parameters, *e.g.* the frequency which has the highest intensity in the power spectrum. These descriptors are listed in table I and fully described elsewhere [17]. Once each signal has been reduced to its mathematical descriptors a variety of different pattern recognition methods may be employed. One such method used in this work is Principal Components Analysis.

The frequency comparison of different acoustic signals can also be achieved by converting the time domain signals collected to power spectra in the frequency domain by using the Fourier Transform. The resulting power spectra of individual signals may thus be compared. Average power spectra for many acoustic signals can also be calculated enabling a comparison in the frequency domain of different acoustic processes.

Table I. Descriptors used to mathematically characterise each acoustic signal.

Time Domain Descriptors	
RMS	Root mean square voltage
PEAK	Maximum voltage amplitude (absolute)
AREA	Integration of the absolute voltages within a signal
CREST	Ratio of peak voltage to root mean square voltage
KURTOSIS	4 th statistical moment (deviation from a Gaussian distribution)
T@AREA/2	Time to half area (signal decay measurement)
50-CROSS	Number of times signal crosses $\pm 50\%$ of maximum voltage
25-CROSS	Number of times signal crosses $\pm 25\%$ of maximum voltage
10-CROSS	Number of times signal crosses $\pm 10\%$ of maximum voltage
0-CROSS	Number of times signal crosses 0 volts
8 TIME OCTILES 1/8T....8/8T	Normalized time octiles of root mean square voltage
Frequency Domain Descriptors	
FRQ MED	Frequency at the mid-area of the integrated frequency intensities.
FRQ MEAN	Frequency equal to the summation of the intensity-weighted frequencies divided by the total intensity
F-CREST	Ratio of the maximum power to the root mean square power
FBW>15%	Bandwidth of frequencies having intensities $> 15\%$ of maximum intensity
FQRTL BW	Bandwidth of frequencies between the second and third intensity integrated quartiles
8 FREQUENCY OCTILES DFB1....DFB8	Normalized area in each power spectrum octile

1.3.2 Principal Components Analysis

Principal Components Analysis (PCA) is a method of finding the set of orthogonal axes which represent the greatest variance in a multidimensional data set. Consider a single acoustic waveform represented by n descriptors. This waveform can be considered as one point in n -space. Now consider many different acoustic waveforms each represented as a single point in n -space. PCA rotates the axes of n -space until a set of axes (principal components) is found that displays the optimal variance in the data set. Display of data using the two or three most important of these orthogonal components, allows data to be easily visualized [18]. The PCA method involves expressing data as linear combinations of the independent contributions, in this case the 32 descriptors. PCA then derives a set of orthogonal basis vectors called principal components, such that each successive principal component describes the maximum amount of variance possible in the data not accounted for by previous principal component's [19]. If two or more acoustic mechanisms with different acoustic signatures exist in the data set being analyzed by PCA, and the bulk of the variance can be accounted for by just a few principal components, the signals of like mechanisms should cluster together on the plane of the data set being displayed (e.g. Principal Component #1 vs Principal Component #2).

1.4 Crystallization Processes

Crystal growth from solution requires the attainment of supersaturation. Once this has been achieved, crystallization can be divided into two main processes, nucleation and growth [20].

1.4.1 Nucleation

For a crystal to grow from solution a stable crystal nuclei must first be present in the solution to act as a growth centre. This stable nuclei must be of such a size that it will not redissolve. This is called the *critical sized nucleus*.

There are two methods for producing critical sized nuclei. Firstly, the process of spontaneous (primary) nucleation which involves the rapid "snap" change of a portion of the solution to form an ordered (crystalline) structure from the solute particles. The production of critical sized nuclei has been studied by Garten and Head using crystalloluminescence [21]. The speed of the volume change within the solution to produce a primary nucleus is less than 5 ns [22], and it has been postulated that this volume change may produce an acoustic wave, in a similar manner to the acoustic emission generated during the martensitic transformation in steel [11]. The anomalous behaviour of the velocity of ultrasonic waves near the freezing point of a substance due to these density fluctuations has been used to calculate the size of the elementary nucleus necessary for the beginning of crystallisation ($\approx 1 \mu\text{m}$ dia.) [23]. However, this result is 100 times larger than that obtained by Garten and Head using crystalloluminescence [21]. Indeed the smaller value is more likely.

The second process involves the production of critical sized nuclei from crystals already present in the solution. Crystals suspended in the solution may impact with the vessel walls or with each other and small pieces of crystalline material can be broken off. These tiny crystalline fragments may be larger than the critical size and thus secondary nuclei are produced. Secondary nuclei may also be produced by the fracturing of any outgrowths of the crystals due to shear forces acting on the crystal produced by agitation of the solution. These processes are termed "*secondary nucleation*". The study of the collision breeding of MgSO_4 crystals by Mason and Strickland-Constable [24] is the definitive work in this area, although more recently significant contributions have been made by Chernov *et al* [25].

1.4.2 Growth

As soon as stable nuclei have formed in a supersaturated or supercooled system they begin to grow. The nuclei grow by adsorbing solute material from the surrounding solution onto the surface of the stable nuclei. Any perturbation in the processes of solute material to the growing crystal, or the interference with the adsorption of material onto the faces of the growing crystal can thus have a profound effect on the growth of a crystal.

1.4.3 Growth Forms

The shape of a growing crystal is determined by the existence of or lack of dominant growth directions. Different crystallographic faces under identical growth conditions may grow at different rates. It is the relative rates of growth of the crystal faces that determine the final crystal habit [26]. Consider the section of three adjacent crystal faces overleaf.

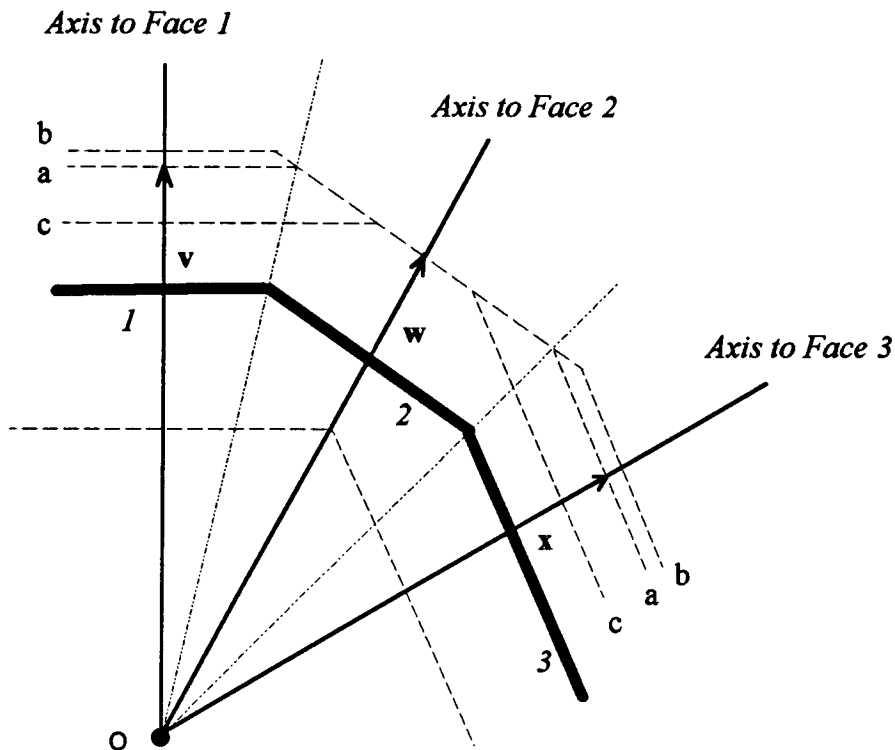


Fig 1. Growth of crystal faces. Adapted from reference [60].

The normal growth rates of the crystal faces are denoted by v , w , and x such that in unit time the faces are displaced to position a . The crystal shapes at each stage of the growth remain similar (position a) providing that $v/w = K_1$ and $x/w = K_2$ (K_1 and K_2 are constants). If the rate of growth of face 1 and face 3 increase such that $v > K_1 w$ and $x > K_2 w$ (position b) then the size of face 2 increases during the growth of the crystal, thus the slowest growing face determines the crystal morphology [27]. If the rate of growth of faces 1 and 3 decreases with respect to face 2, then the size of face 2 decreases (position c). One common method of anisotropically affecting growth rates of crystal faces is the introduction of impurities into the system [28].

1.5 Effect of Impurities on Crystal Growth

Any substance other than the material being crystallized can be considered an impurity. Some impurities can suppress growth entirely, some enhance growth, while others produce a highly selective effect, acting on certain crystallographic faces only, and thereby modifying the crystal habit (as above). The quantity of impurity necessary to influence crystal growth varies from system to system, with some impurities exerting an influence at concentrations as low as fractions of ppm (such as is the case for the ferrocyanide ion in changing the habit of sodium chloride [29]), while others require much larger concentrations of up to 1000's of ppm.

Impurities influence the growth of crystals by a variety of methods. The introduction of an impurity can change the properties of the solution (sometimes structurally) [27], or they can alter the adsorption layer at the crystal solution interface [26]. They may be selectively adsorbed onto certain crystal faces exerting a blocking effect, or be incorporated into the lattice [30]. Some impurities may interact chemically with the crystal and selectively alter the surface energies of different faces. Recent research has focussed on this last mechanism producing a number of 'tailor made' organic additives that are designed to selectively adsorb onto certain surface sites of growing organic crystals and thus retard growth selectively in the x, y or z direction. One such system where this control is possible is for the influence of L-glutamic acid on the growth of L-asparagine [31]. Even the solvent of the crystallizing system is strictly an impurity [28], and indeed changing the solvent frequently results in a change of crystal habit and growth kinetics [32, 33].

The modification of crystal habit is of great importance in industry, and not just of academic curiosity. Certain crystal habits are desired because of their anti-caking

characteristics, and good flow capabilities. General handling and packaging of materials can also be aided by the correct choice of crystal habit [34, 35]. For certain applications the rate of dissolution of the crystal is crucial (*e.g.* washing powders, pharmaceuticals); and this is an area where the habit of the crystal and specifically the surface area to volume ratio can again have a significant effect.

1.6 Crystal Growth Monitoring

Many methods have been used to follow crystal growth. The methodologies used to follow crystal growth are diverse, as it only requires the measurement of a single component related to the growing crystal [36]. Direct optical measurements of particular face growth rates [37-39] are used to follow the growth of different single crystal habits, while crystal size distribution measurements have been used to follow batch crystallizations [40]. Indirect methods such as raman microscopy [41], refractometry [42], light scattering [43] and potentiometry [36] have also been employed to monitor the uptake of solute material from solution. Synchrotron radiation is now being used to probe the crystal solution interface in-situ. This work has been pioneered by K. J. Roberts [44].

With the advent of more powerful personal computers in the laboratory, automated image collection techniques are superseding the manual observations of face growth rates. Slow crystal growth techniques such as vapour diffusion lend themselves to this type of monitoring [45]. Time lapse photography has been used by McPherson *et al* to follow the growth of lysozyme [46]; digital image capture methods have been developed by Rosenblum *et al* [47] for following the growth of lysozyme aboard the NASA space shuttle.

1.7 Acoustics and Crystallization

Sound has been used as an external structural probe for single crystals [48-50] and solution composition near the freezing point [23], but acoustic emission has largely been overlooked for monitoring crystallization. Betteridge *et al* first reported the emission of acoustic signals from the recrystallization of KCl in 1981 [51], but little work has been done since. A study of bulk precipitation of dichloro(pyrazine)zinc(II), a crystalline inorganic polymeric material, from solution was carried out by Munro [53]. Munro attributed the source of acoustic emission purely to the gross fracture of crystals suspended in solution due to inter-particle collision, or contact with the vessel walls: in other words, the very processes of secondary nucleation. Bulk recrystallizations have attracted some interest from acoustic emission researchers, as the processes of secondary nucleation should be amenable to acoustic monitoring [52]. The non-invasive nature of AE would be a great advantage when following the kinetics of secondary nucleation in industrial crystallizers, as at present they have to be regularly sampled, and crystal size distributions calculated.

Several workers have reported acoustic emission from the crystallization of polymers from the melt [54-56]. They identify the source of the acoustic signals as the abrupt negative pressure release in regions of the melt occluded by spherulites during crystallization. This mechanism involves the release of stress from within a solid matrix, a common source of acoustic emission. The crystallization of metallic glasses from the melt has also been studied, and a similar mechanism proposed [57].

Lube *et al* have used acoustic emission to study the perfection of single crystals during melt growth [9]. They attributed the emission to a variety of solid state processes including, dislocation pile-ups, slipping, twinning, inclusion movement and cracking.

While these emissions gave an indication of the ideality of the crystal grown, the number and regularity of the acoustic signals were not sufficient to provide an acoustic method which could monitor the rate of growth of a single crystal.

The first attempt to detect acoustic signals from morphological changes of crystals due to the addition of impurities was made by Delly [58]. He attempted to acoustically detect the change of habit of sodium chloride on the addition of urea, but without success. The bandwidth used however, was limited by the equipment available to a very low frequency range (3-16kHz, audible frequency range). Differences in acoustic signals from growth of various morphologies of crystals were briefly mentioned by Sawada et al [6] who noted that formation of *plural* crystals during the precipitation of sodium thiosulphate generated the most intense acoustic signals.

1.8 Crystal Growth of KBr

The ionic alkali metal halide KBr, under normal conditions, has a face-centred cubic unit cell according to the simple electrostatic model.

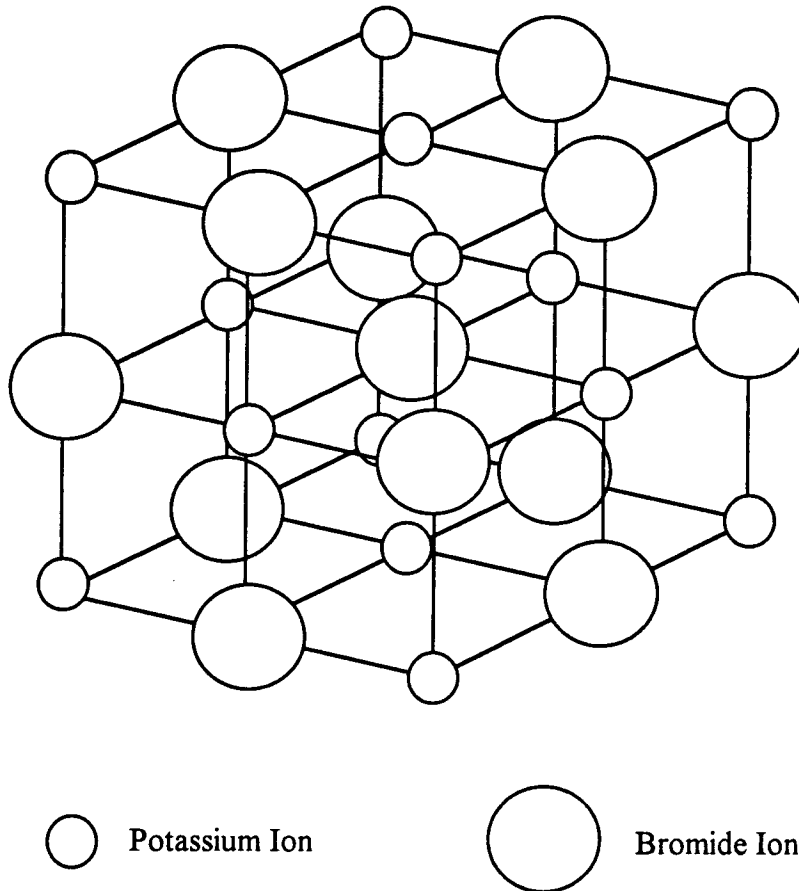


Fig 2. Unit cell of potassium bromide.

The potassium ions and bromide ions are both in face-centred cubic arrangements so that the lattice consists of two interpenetrating face-centred cubic lattices [59]. The co-ordination number of both ions in the lattice is six. The habit of KBr crystals growing from a pure solution is thus hexahedral, with dominant bounding faces of $\{100\}$.

There are many methods whereby KBr can be persuaded to crystallize in forms other than cubic. If the evaporation rate is too fast the growth layers follow each other so quickly that the central parts of the crystal are not filled, and the result is termed "*skeletal growth*" [60]. This can be produced by changing the solvent from pure water to a mixture of water and alcohol. A further increase in evaporation rate can result in the dendritic growth of KBr [60].

Classic dendritic growth consists of a main stem from which primary and secondary branches grow. Many compounds exhibit this type of growth (*e.g.* NH_4Cl [60]). It usually occurs in one plane, with very regular spacing of the branches. The dendrites are single crystals with the branches following definite crystallographic directions. This mode of growth is still not well understood.

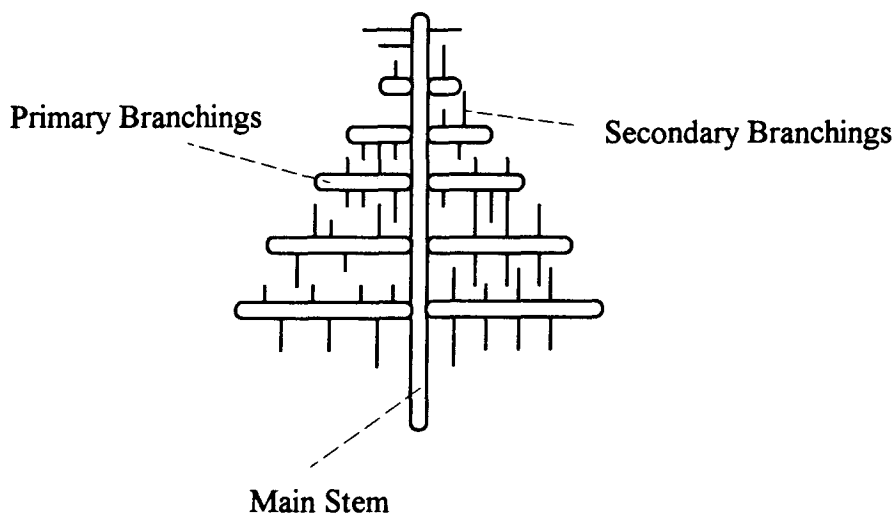


Fig 3. Classic dendritic growth.

The growth of KBr whiskers, microfine (1-10 μm) single crystals which grow in one direction only, is also possible [60]. Polyvinyl alcohol has been reported as an impurity that enhances the formation of KBr whiskers from evaporating solutions,

whereas lead impurities such as lead nitrate inhibit the formation of KBr whiskers [60]. Whiskers can also be produced by mechanical agitation of the crystallizing vessel as a saturated solution of KBr cools while sealed. An "avalanche" of tiny crystals is seen within the solution [60]. Mechanical agitation is a common method of initiating primary nucleation.

Changing the evaporation rate to produce different KBr morphologies is not easily controllable. However, the doping of KBr crystallizing solutions with varying amounts of impurity can give fine control of the crystal habit.

1.8.1 Effect of Lead Impurity

The cubic to octahedral change of KBr on the addition of Pb impurity has long been known. A recent study by Agarwhal *et al* showed that as the lead content of a crystallizing solution of KBr is increased from 0-4000 ppm, {111} faces appear, together with the {100}, until eventually they become the dominant bounding faces [61]. The crystal habit of KBr has thus been changed to octahedral.

The mechanism by which the lead impurity affects the growth of KBr is one of selective adsorption. This is explained using the model proposed by Sears [62]. The lead impurity is adsorbed on the growth steps of the {111} face. The growth rate from a step is then controlled by the equilibrium concentration of single unfilled sites in the line of adsorbed atoms. As the concentration of the lead increases the number of vacant sites along each step decreases and thus the rate of step motion is itself decreased. As indicated previously, it is the slowest growing face that dominates the crystal habit. The retardation of the {111} face thus produces an octahedral habit from the original cubic habit.

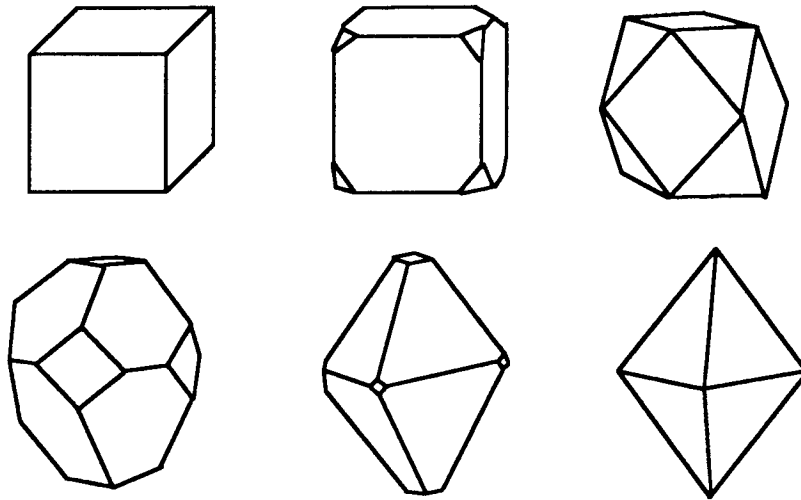


Fig 4. Schematic representation of the change in habit of KBr from cubic to octahedral on the addition of lead impurity. Adapted from reference [61].

A further increase in the level of Pb impurity to $\approx 1\%$ led to the observation of a finger-like growth of KBr [60]. This was termed the growth of KBr 'dendrites' by the authors, although the growth observed was not classic dendritic growth. Indeed the individual dendritic branches were seen to run forwards from the evaporating droplet, sometimes rising above the surface by 1-2mm. The branches were observed to be irregularly spaced and twisted in many different directions. The crystal morphologies of KBr grown from solutions containing more than 1% lead dopant have not been reported.

1.9 Purpose of the Present Work

The goals of the present research have been three-fold. Firstly, to better understand the origins of AE during crystal growth. To facilitate this the investigation of different modes of growth of crystals by using simultaneous optical and acoustic monitoring was carried out. By comparing the rate of acoustic emission to the rate of crystallization information about the acoustic mechanism was sought. Secondly, to ascertain if there were any differences in the acoustic activity and signal characteristics of acoustic waveforms emitted during the crystallization of these different crystal morphologies. To date a successful study linking acoustic activity and crystal morphology has not been completed. Thirdly, to compare the signals emitted during crystal growth with signals designed to mimic processes that may occur during secondary nucleation, and thereby assess the practicability of monitoring crystallization processes by acoustic emission.

Primarily, one system was used for this study: KBr grown from solution by evaporation. The KBr solutions were doped with varying degrees of lead impurity that enabled many different crystal morphologies to be grown. A second system, NH_4Cl grown by evaporation, produced classic dendritic growth. These experiments were done for comparison with the finger-like growth of KBr dendrites [60]. Primary nucleation was studied by producing copious numbers of KBr whiskers by mechanical agitation. This sought to determine if the generation of the critical sized nucleus was acoustically emissive.

II EXPERIMENTAL

2.1 Reagents

All the chemicals used were analytical grade unless otherwise stated. Potassium bromide (KBr, 5 ppm lead impurity max) was obtained from BDH Chemicals (Toronto, ON). Lead nitrate ($\text{Pb}(\text{NO}_3)_2$, 99%+) and ammonium chloride (NH_4Cl , 99%+) were obtained from the Aldrich Chemical Company (Milwaukee, WI).

2.1.2 Solution Preparation

The solutions were prepared saturated at 20°C, just below room temperature, to ensure a short evaporation time at ambient temperature before the solution became supersaturated and crystals began to form. Three separate series of KBr solutions doped with varying degrees of lead impurity were prepared by weight (± 0.0005 g) using an analytical balance (model H10, Mettler, Greifensee, Zurich).

KBr Series #1: 6 solutions of KBr with 0 ppm, 600 ppm, 1010 ppm, 2080 ppm, 2750 ppm, and 4920 ppm Pb dopant.

KBr Series #2: 14 solutions of KBr with 0 ppm, 670 ppm, 1050 ppm, 1990 ppm, 4080 ppm, 6070 ppm, 8020 ppm, 12210 ppm, 16000 ppm, 19960 ppm, 22060 ppm, 24840 ppm, 27790 ppm, and 31960 ppm Pb dopant.

KBr Series #3: 11 solutions of KBr with 0 ppm, 770 ppm, 2070 ppm, 3980 ppm, 5900 ppm, 7620 ppm, 11930 ppm, 15980 ppm, 20090 ppm, 24920 ppm, and 29790 ppm Pb dopant.

Further Solutions for KBr whisker growth and the dendritic growth of NH_4Cl were prepared.

Solution #1: KBr, undoped, saturated at 70°C

Solution #2: NH_4Cl , undoped, saturated at 20°C

All solutions were sealed and stored in the dark for the duration of each individual study.

2.2 Apparatus

The various experimental apparatus and instrumentation used are outlined in the following sections (2.2.1-2.2.7). A schematic of the combined apparatus for image acquisition and acoustic emission acquisition is shown in fig. 5.

2.2.1 Image Acquisition Apparatus

A continuously focusable microscope (CFM) (Infinity Photo-Optical Company, Boulder, CO) with a camera (VK-C150, Hitachi) attached was used to collect the images. The CFM focuses continuously from infinity down to 6 mm. The primary magnification is dependent on the distance of the lens from the sample. The camera is based on a solid state image sensor ($8.8 \times 6.6 \text{ mm}^2$, 11mm diagonal), and outputs a standard video signal. The video signal output was fed into a frame grabber card (PCVisionplus, Imaging Technology Inc., Woburn, MA) in a host microcomputer (PC/AT) and digitized. The digitized image, 640 x 480 pixels, 256 grey scale (8-bit), was then displayed on a

monochrome monitor (330mm diagonal, Sync Master II, Datatrain, Roland DG Canada Inc.). This image was updated according to a time delay specified by the operator (see section 2.2.2) Samples were illuminated with an optic fibre light source (Cambridge Instruments Inc., Buffalo, NY) which imparted very little heat to the sample. Indirect partial dark field illumination was used to prevent any intense white spots being created by reflections from the sample surface.

The total magnification produced by the CFM was calculated as follows:

$$\text{Total Magnification} = \text{Primary Magnification} \times \text{Aspect Ratio}$$

(solid state sensor to monitor)

For the system used here the aspect ratio is x30 (330 mm / 11 mm), and the primary magnification varies in a linear manner with the distance of the lens from the sample, with values of x0.2 at 152 mm, to x9 at 6 mm. This scale is not linear, with the greatest rate of change at the shorter distances, and so the magnifications quoted in this thesis were calculated directly by measuring the dimensions of the image from an object of known size. When the method of calculation outlined above was used it varied by $\pm 10\%$ (relative) from the value calculated by measuring the dimensions.

The video signal output from the camera was also simultaneously fed into a colour monitor (KV-2064R, Trinitron, Sony Corp.) via a standard VHS VCR unit (HR-D670U, JVC). The colour monitor displayed the real-time image, so that the operator could easily follow the crystallization, and the VCR enabled subsequent review (see fig. 5).

2.2.2 Software Development for Image Acquisition

A routine was written in the 'C' programming language to control the frame grabber, allowing the user to acquire a specified number of images (maximum of 1000) with a specified time delay between each image (minimum of 3 s). This routine also performed a near real-time pixel summation of the grey level values across the entire image to quantify the whiteness of the image. This value was then stored along with suitable image identifiers such as the image number and time of acquisition as an ASCII file. As each image required approximately 307kB of memory for storage only selected images (*e.g* every 50th) were permanently recorded on disk for later visual analysis and display. The routine allowed for a baseline correction to ensure that the grey scale was not saturated by the whiteness of the sample (the maximum whiteness of a single pixel = 255). The whitening of the image was used as an independent method of following the crystallization. This enabled the acoustic activity to be compared to a reference.

2.2.3 Apparatus for Acoustic Emission Detection

The acoustic signal detector used for all the experiments was a broad-band piezoelectric transducer (model 8312, serial# 1381660, Bruel and Kjaer, Naerum, Denmark). This transducer contained a piezoelectric crystal sensor ($\approx 1.5 \text{ mm}^2$) and an internal preamplifier of 34 decibel (dB) gain. The manufacturer's frequency response curve for the transducer, and a background blank recorded in the laboratory are given in fig. 6. For the background blank a trigger level of 0 V was set and signals were recorded every 2 s for a period of 5 min. The transducer was mounted on a piece of foam matting (25 mm) to damp out unwanted laboratory vibrations.

The output from the transducer was directed to a conditioning amplifier (model 2638, serial# 1283189, Bruel and Kjaer) with a variable gain of 0-60 dB, and a bandpass filter of 50kHz-2MHz. The conditioning amplifier had two outputs, an a.c. output which produced the conditioned transducer signal (a representation of the acoustic waveform) and a d.c. output which gave the damped peak amplitude of the transducer signal. All acoustic data that were collected were normalized to a total gain of 64 dB (34 dB preamplification, 30 dB main amplification) so that quantitative comparisons could be made.

2.2.4 Modes of Acoustic Acquisition

Two methods of acoustic monitoring and quantitation were used in this study, thus utilizing both the a.c. and d.c. outputs of the conditioning amplifier.

2.2.5 Acoustic Emission Integration

This method involved the collection of the peak d.c. amplitude output via a 12-bit analog to digital convertor (model RTI-815F, Analog Devices, Norwood, MA) in a second host microcomputer (Compaq model II (PC/XT), Compaq Computer Corp., Houston, TX). Software developed within this laboratory samples this d.c. output and integrates it over time. This has been reported previously [63], so only a brief description will be given here.

The software developed enabled the peak d.c. amplitude to be collected every 40 ms and then averaged every 20 points. This produced one data point every 0.8 s, corresponding to the acoustic emission intensity observed in that 0.8 s time window. The data provided a method of following the *rate of acoustic emission* and gave a measure of

the total acoustic emission collected during the experiment. Before each experiment a baseline was measured over a period of 10 min. The baseline level was automatically subtracted from the levels obtained for the real signals. Real signals were then collected by means of a trigger level that was set at three times the standard deviation of the baseline readings.

2.2.6 Individual Acoustic Signal Detection and Collection

Acoustic waveform data were collected from the a.c. signal output of the conditioning amplifier using a fast digitizer (model SDA2000, Soltec Inc., San Fernando, CA). Each signal was represented by 1024 points, 992 points for the signal plus 32 pre-trigger points, with 12-bit resolution. Two sampling rates were used 2.5 MHz and 5 MHz, and the trigger level was set to 1.5 times the background noise level. The background level was determined by finding the trigger level voltage at which the transducer barely detected acoustic signals in the open laboratory over a period of 10 min. The background was determined prior to every experiment. The digitized signal was then transferred to a host microcomputer (PC/AT) via an IEEE-488 interface (model PC IIA, National Instruments, Austin, TX) and stored on the PC/AT hard drive for later analysis. The data acquisition program used was developed in this laboratory and has been reported elsewhere [64]. Simultaneous acoustic waveform analysis and image acquisition was impossible using the experimental arrangement described, as the same PC/AT was used for both the data acquisition from the fast digitizer and image acquisition using the frame grabber card (see fig. 5).

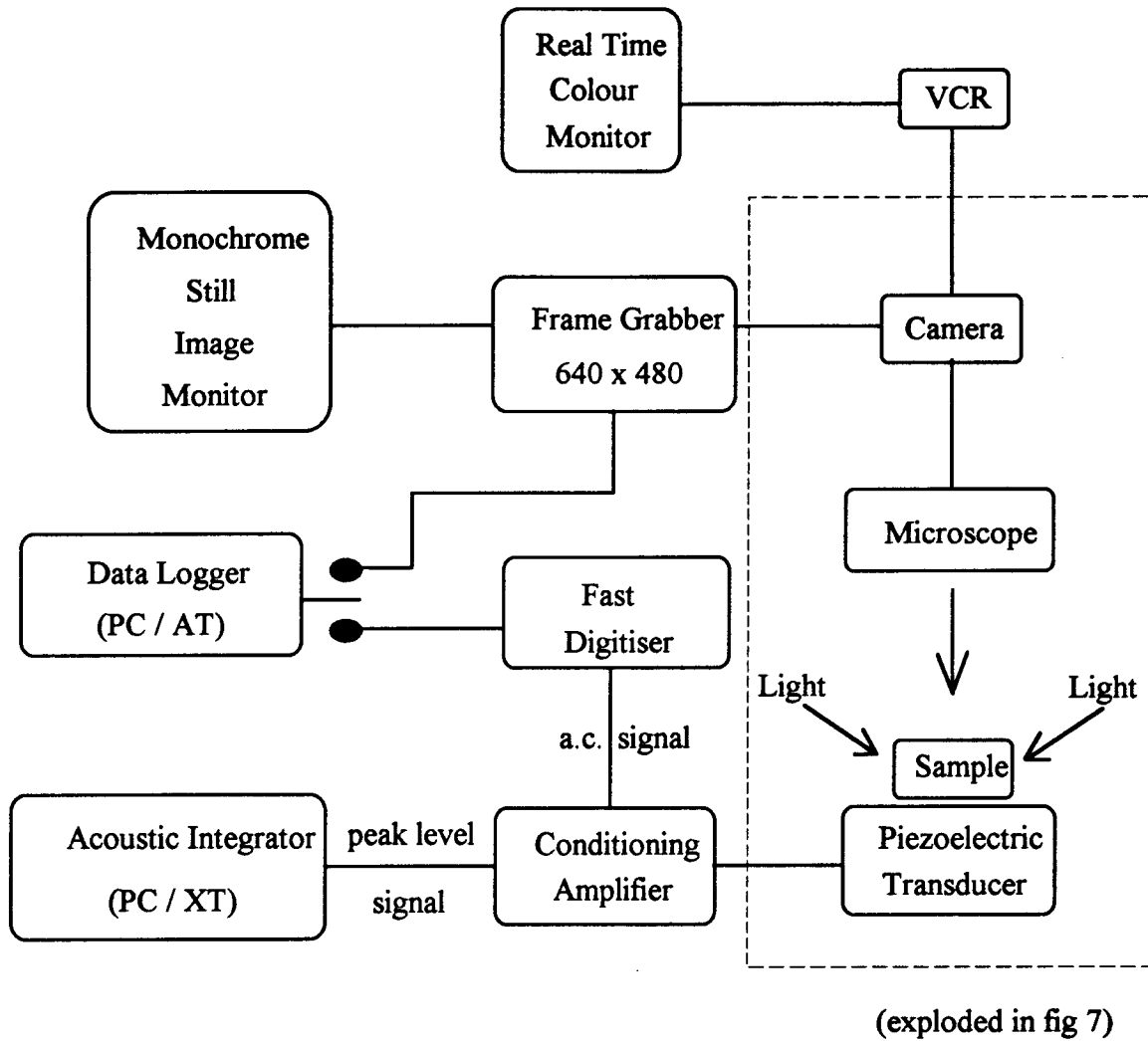


Fig 5. Apparatus schematic.

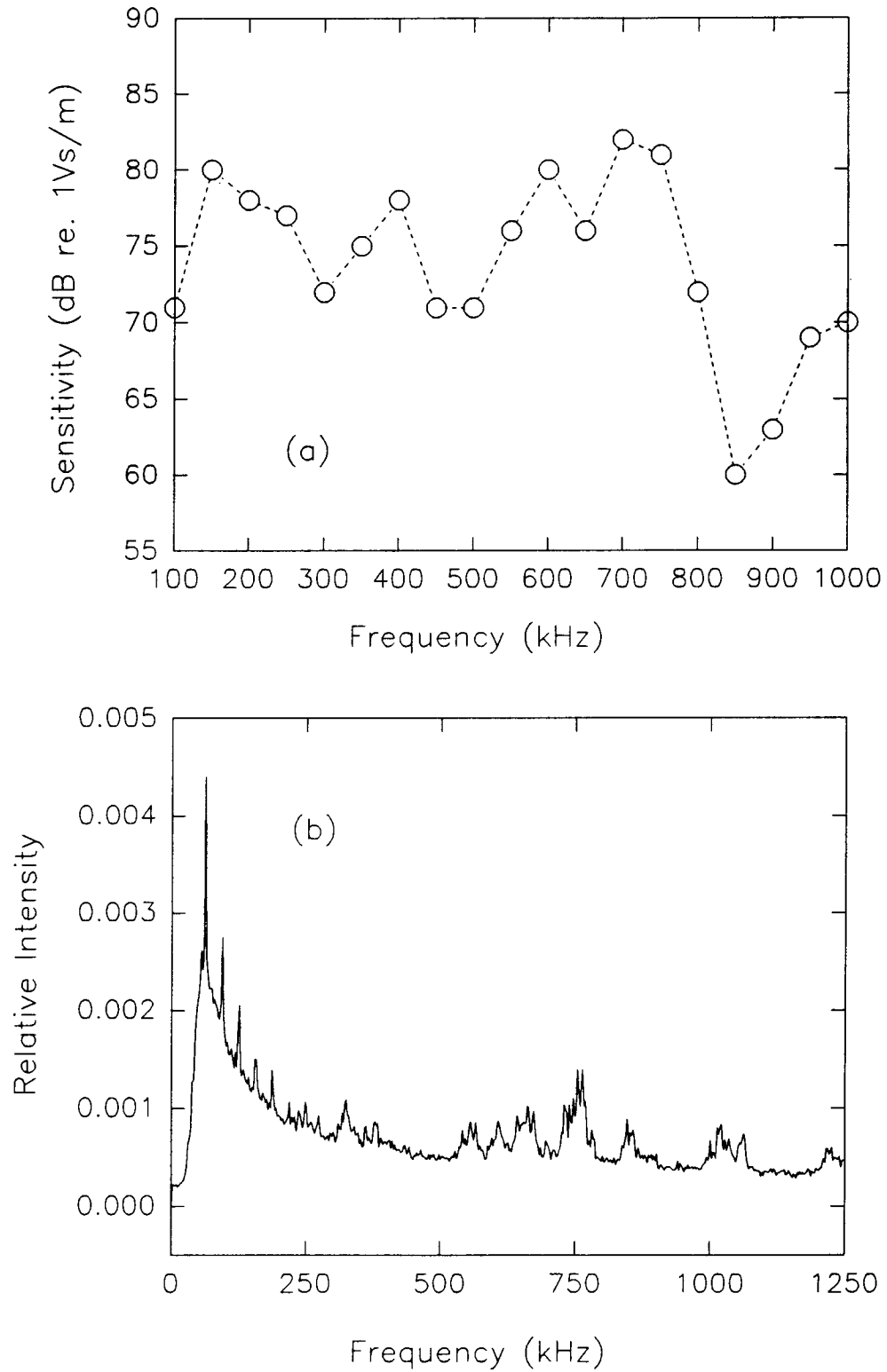


Fig 6. (a) Transducer's frequency response curve,
(b) Background frequency spectrum of blank.

2.2.7 Ex-situ Analysis Methods

Ex-situ analysis of the crystal morphologies grown were investigated using scanning electron microscopy (SEM) (0.01 μm resolution) (S2300, Hitachi). An accelerating voltage of 20 kV was used with the detector at a working distance of 15 mm. Energy dispersive X-ray analysis (EDX) (S570, Hitachi) was used to determine any spatial variations (1 μm resolution) in chemical composition for the morphologies grown. The working distance of the detector was 35 mm with an identical accelerating voltage as the SEM settings.

Samples for SEM and EDX analysis were prepared as follows. The KBr crystals doped with Pb were carefully removed from the transducer surface and mounted on aluminium holders using adhesive applied from a removeable label. The samples were gold coated to provide an electrically conductive surface to facilitate analysis by SEM and EDX. The gold coat was deposited under a reduced pressure (100-200 mtorr) argon atmosphere, with a direct current of 20 mA. The exposure time used was 4 minutes, resulting in a 100 Å thick coating.

Structural features of the morphologies grown were identified using a magnifying glass and removed from the transducer with tweezers. These crystal samples were then ground, mounted on a microscope slide using vaseline, and analyzed by powder X-ray diffraction (XRD) (Rotating Anode machine, Cu target, $K\alpha_1 = 1.5418 \text{ \AA}$; Rigaku USA Inc., Danvers, MA). The X-ray tube current and tube voltage used were 150mA and 60 kV respectively. The XRD served to confirm variations in chemical composition of the different structural features indicated by EDX analysis.

2.3 Experimental Procedure

The following sections give the experimental arrangements and procedures used for the different crystallization studies.

2.3.1 General Procedure for KBr Morphological Studies

A droplet of the KBr solutions doped with lead impurity was placed on the upper stainless steel surface of the transducer and allowed to evaporate at ambient temperature ($23 \pm 2^\circ\text{C}$) (see fig. 7). Solutions were selected in no particular order until one trial had been completed for each solution in the given series. This process was repeated until at least 3 replicate experiments of each solution had been completed. This procedure was adopted to minimize variations across the series due to changes in ambient conditions.

The growth of the crystals was monitored acoustically using the integration method (section 2.2.5) for a period of 4 hrs. The total acoustic emission was then recorded, normalized to the mass of crystals produced, and an AE vs. time trace obtained. The results for replicates were averaged. Prior to each crystallization experiment the transducer was thoroughly cleaned with de-ionized water to remove all residual crystalline material which might form unwanted sites for nucleation in future experiments. Acetone was used to remove any grease build-up and ensure comparable wetting of the transducer surface for each experiment.

2.3.2 Preliminary Experiments

Initially the KBr / Pb(NO₃)₂ system was investigated over the dopant range of 0-4920 ppm Pb using the solutions of series #1. The procedure was as outlined above. No microscopic imaging or ex-situ analysis was carried out. A large range of droplet sizes was tried, 50-250 μl.

2.3.3 Complete Morphological Study

A comprehensive study of the KBr / Pb(NO₃)₂ crystallization was carried out over the dopant range of 0-31960 ppm Pb using the solutions of series #2 and series #3.

2.3.3.1 Acoustic Integration and Optical Imaging

Simultaneous microscopic observation with image collection and acoustic monitoring (see general procedure) was carried out (see figs. 5, 7). A typical image seen through the microscope is shown in fig. 8. The crystallizing solutions of series #2 were used. Studies were completed with magnifications of x20 and x75. Droplet volumes of between 4-100 μl, were used depending on the degree of magnification and the amount of spreading expected during the growth of each different crystal morphology. These were dispensed via a precision syringe (± 1μl) (Hamilton Co. Inc., Whittier, CA). Exact volumes are discussed later. Comparisons were then made of the acoustic emission integration trace with time vs. the image whitening trace with time to gain an insight into the acoustic emission generation mechanism.

The ex-situ analysis of each morphology grown was carried out using the techniques outlined in section 2.2.7.

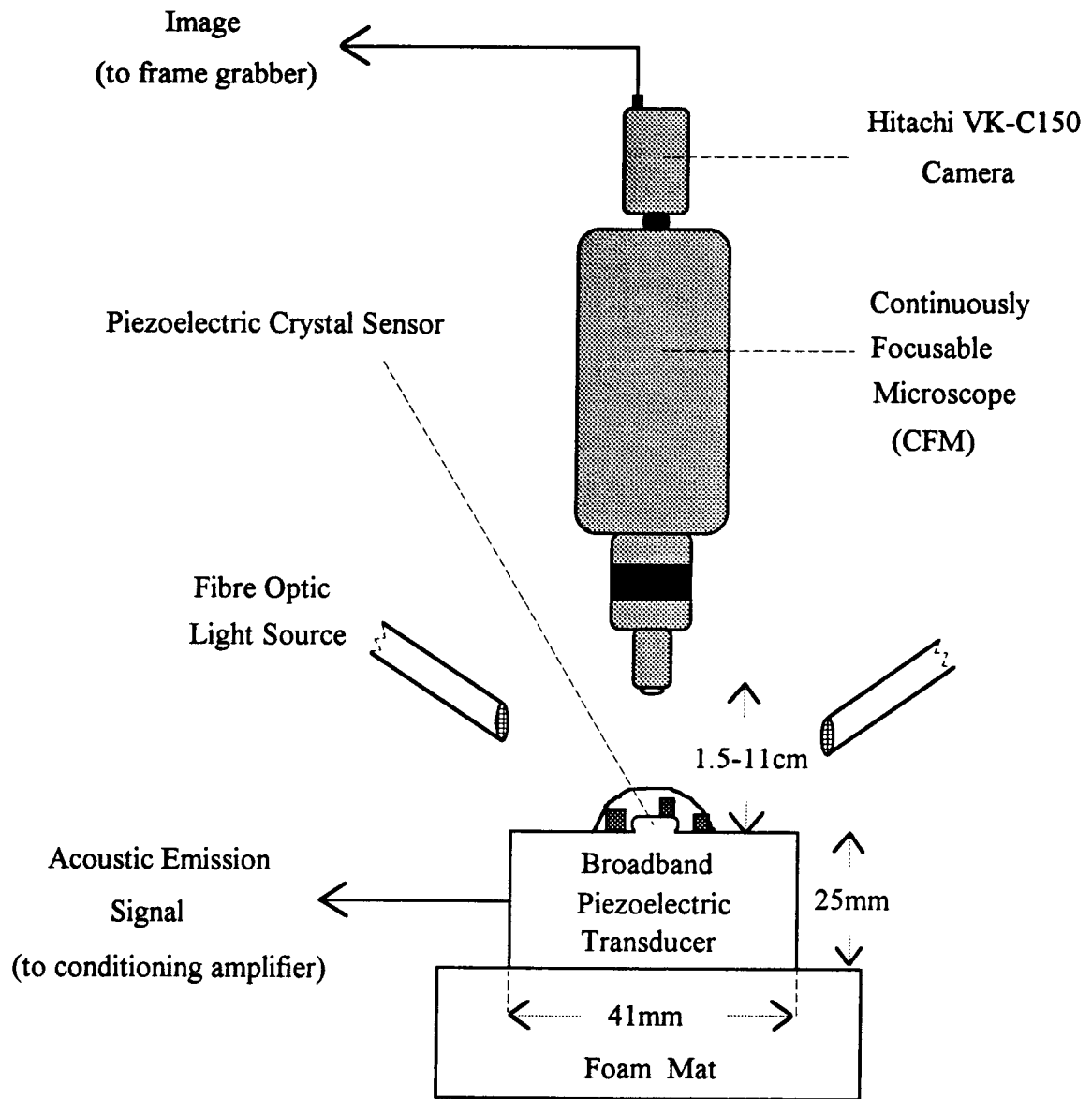


Fig 7. Arrangement used for crystal growth experiments.



Fig 8. Typical image of cubic KBr crystals on the surface of the transducer. Image viewed through a continuously focusable microscope with a magnification of x20.

2.3.3.2 Capture of Acoustic Waveforms Arising During Crystal Growth

The solutions of series #3, similar in composition to series #2, were used as a source of acoustic waveform data during growth. These experiments were done without simultaneous image acquisition. Experiments were of 4 hrs duration, and the apparatus used was as outlined in section 2.2.6. Two frequency bandwidths were used for signal collection and analysis, 1.25 MHz and 2.5 MHz. The signals collected during growth were then compared by using PCA to determine if there were any differences between the growth signals of different KBr morphologies.

2.3.4 Artificially Produced Acoustic Signals from Crystallization Processes

Artificial signals of bulk fracture and impact were produced to mimic the processes of secondary nucleation. Bulk fracture signals were produced as follows; the fingers of the dendritic form of KBr obtained with 7620 ppm Pb dopant were fractured with the aid of a syringe needle. Impact signals were produced by dropping a variety of different sized KBr particles (0.1-0.5 mm) from heights of between 2-3 cm onto the surface of the transducer. These signals were compared with the growth signals using PCA. A frequency bandwidth of 1.25 MHz was used.

2.3.5 Primary Nucleation Study

A primary nucleation study was carried out by producing a large number of tiny KBr whiskers using mechanical agitation. The method used was as follows. A 50 ml graduated cylinder was filled to 2/3 of its height with solution #1. A thermometer was placed in the graduated cylinder and the tube sealed using parafilm to prevent the entry of dust particles and limit evaporation. The solution was then heated to 80°C to fully

dissolve any KBr, and then mounted on the transducer surface using apiezon grease (Apiezon Products Ltd., London, U.K.) as an acoustic couplant (fig 9). When the temperature had reached 68°C the tube was tapped with a wooden block to induce mass nucleation. This primary nucleation was monitored acoustically as outlined in section 2.2.6.

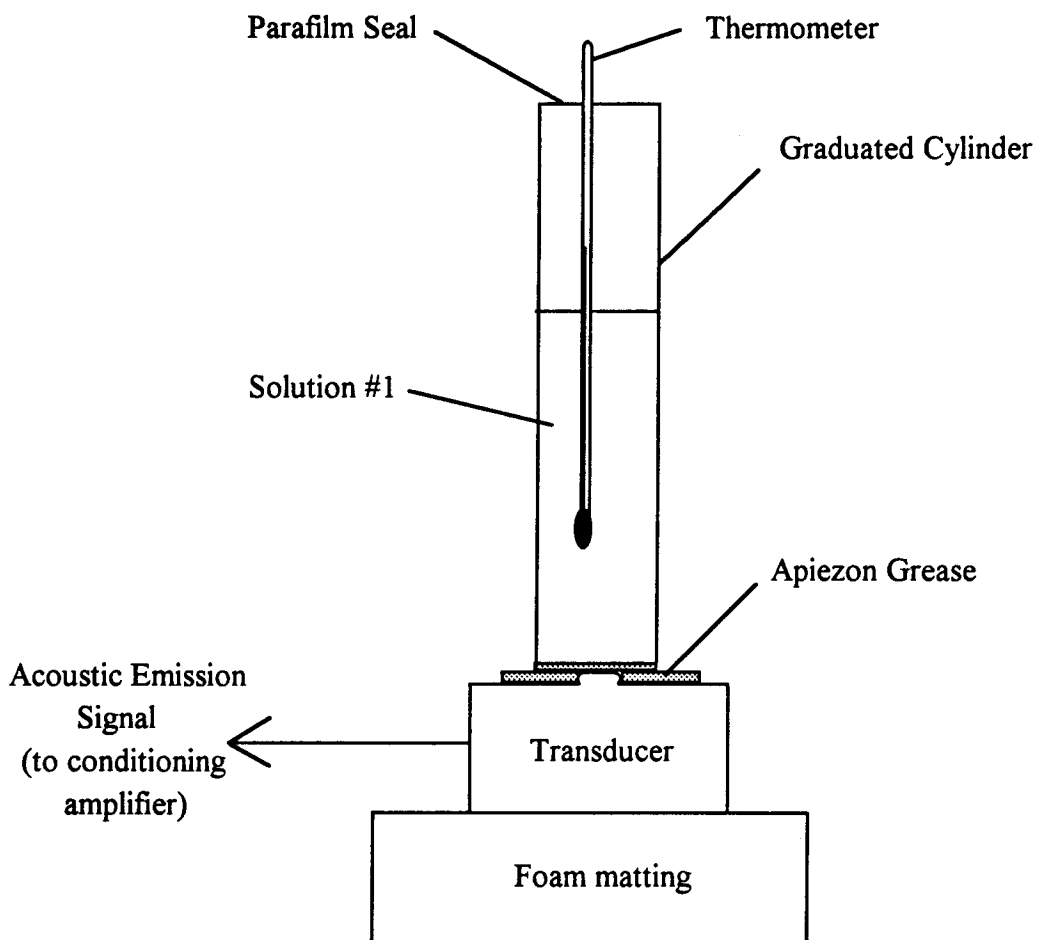


Fig 9. Experimental arrangement for KBr whisker formation.

2.3.6 Dendritic Growth Study

Classic dendritic growth was produced using a solution of NH_4Cl , solution #2 (section 2.1.2). The general procedure outlined in section 2.3.1 was used to monitor this dendritic growth.

2.4 Data Analysis Methods

The different methods of data analysis used during this study are outlined in the following sections.

2.4.1 Integrated Acoustic Emission and Image Whitening Analysis

The integrated acoustic emission profiles were first converted to an ASCII format. The traces of integrated acoustic emission with time and image whitening with time were then compared directly on the same plot using a commercially available graphing package (Sigmaplot, version 5.0, Jandel Corporation, Sausalito, CA). The time taken for the curves to rise from 10% to 90% of the final value were calculated and used to compare the rise times of the AE profile and the image whitening profile.

It is pertinent to mention here the units that are used to represent the acoustic emission data in this thesis. There is no standard reference measure (calibrant) for acoustic emission, and SI units of acoustic emissivity do not exist [64]. This has led to acoustic emission being measured using a variety of different methods, with the signals observed strongly dependent on the equipment used. The acoustic emission data in this study has thus been given arbitrary units (AU), with all scales comparable.

2.4.2 Acoustic Waveform Analysis

All the software for signal processing and analysis was written in this laboratory and has been reported elsewhere [65]. Before any generation of descriptor information or frequency power spectra, all over-ranged and under-triggered signals were removed from the data set. Over-ranged signals have amplitudes that exceed the voltage range selected for collection, while under-triggered signals are a result of trigger level instability. Neither of these signal types are desirable. Power spectra were calculated by the using a fast Fourier Transform to convert the time domain signal to the frequency domain. The average power spectrum was then calculated; this is an average of the individual frequency intensities of each signal. Descriptor information was calculated for each signal collected in order to characterise the signals. These descriptor values were then used for PCA.

Prior to PCA, one of each pair of descriptors that was found to correlate with each other at a level greater than 90% was removed. Obviously, descriptors that correlate highly with each other will not add significant information to the variance within the data set. Those that were found to have a poor resolution across the different classes of signals under study, *i.e.* descriptors that have a poor separation capability, were also removed prior to PCA. Only 18 of the 32 descriptors were thus used (see table V) to separate the different signal classes. Assignments of signal classes to the different data sets will be given later.

The descriptors were then autoscaled and link-scaled [18] to correct for changes in variance in the time octiles and frequency octiles (see table I). A plot of any 2 of the principal components generated could then be used to view signal clustering within the data set (see fig. 10).

For improved separation of the different classes of signals the three descriptors with the highest resolution across the data set were determined. The data set was then re-analyzed by PCA. The removal of all the independent contributions (descriptors) except three decreases the total variance across the signals of individual classes within the data set, and proved adequate for separation in most cases.

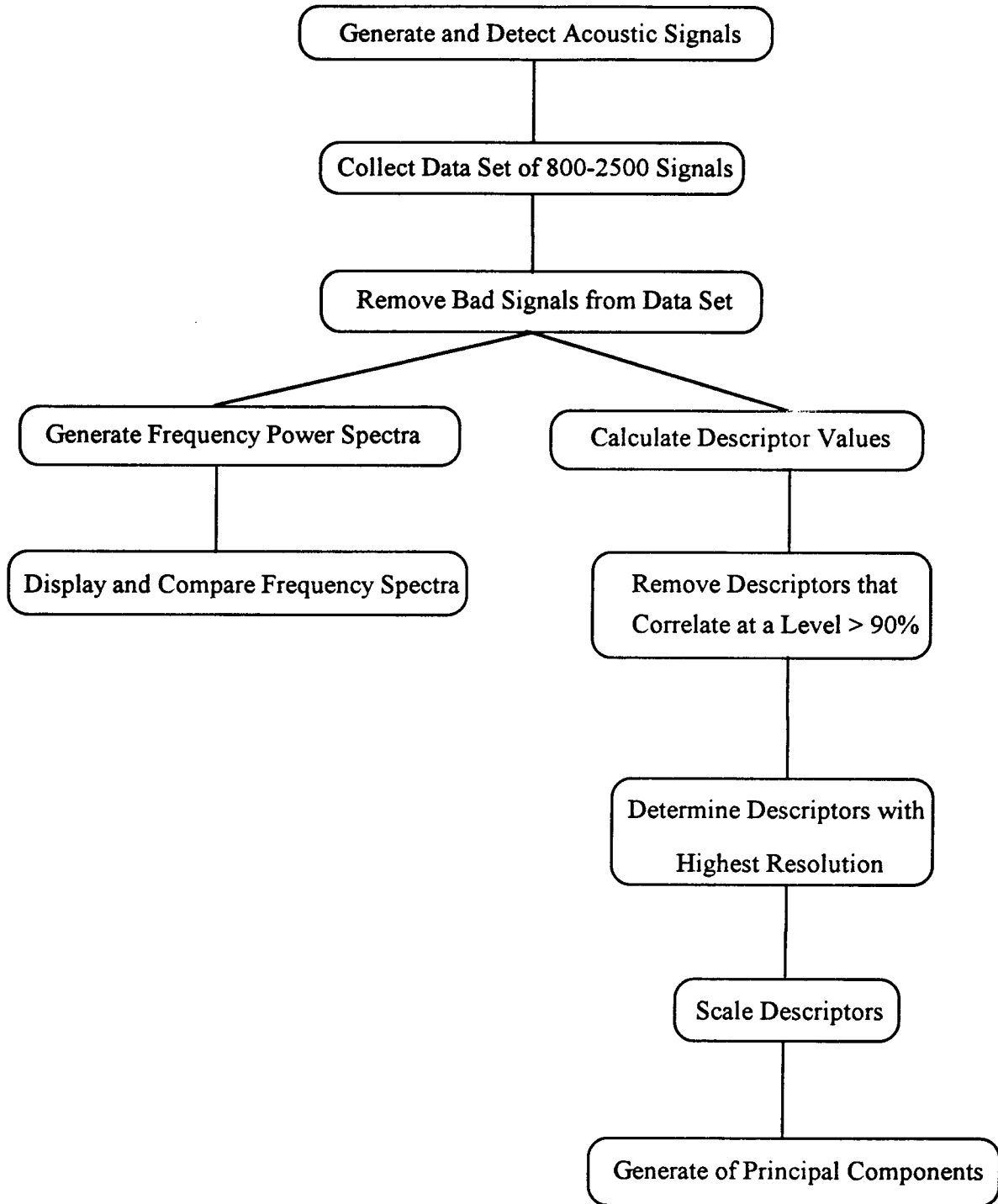


Fig 10. Data analysis strategy for acoustic waveforms collected during crystallization processes.

III RESULTS AND DISCUSSION

3.1 Findings of Preliminary Morphological Study of KBr

The KBr crystal forms grown during the preliminary study (solutions of series #1) were visually seen to change from a hexahedral habit with 0 ppm Pb through an octahedral habit, until at the highest dopant level examined, 4920 ppm Pb, the growth of irregular twisted fingers was observed. These fingers spread out rapidly from the droplet until the entire surface, and in some cases even the sides, of the transducer were covered. Some of the fingers rose off the surface of the droplet by as much as 0.5 cm, in agreement with previously reported work [60]. The crystals of the cubic and octahedral morphologies of KBr grown stayed within the boundaries of the initial droplet.

KBr finger-like growths

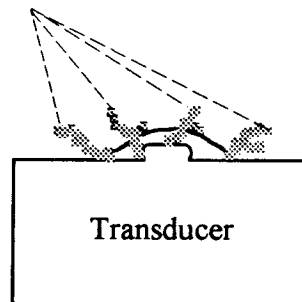


Fig 11. Dendritic form of KBr crystals observed with 4923 ppm Pb dopant. Growth of fingers on the transducer surface.

3.1.1 Trends in Integrated Acoustic Emission

The total acoustic emission (normalized to the mass of crystals grown) as measured during the growth of each of these different forms of KBr was found to increase with Pb dopant (see fig. 12). This trend was observed to varying degrees for each

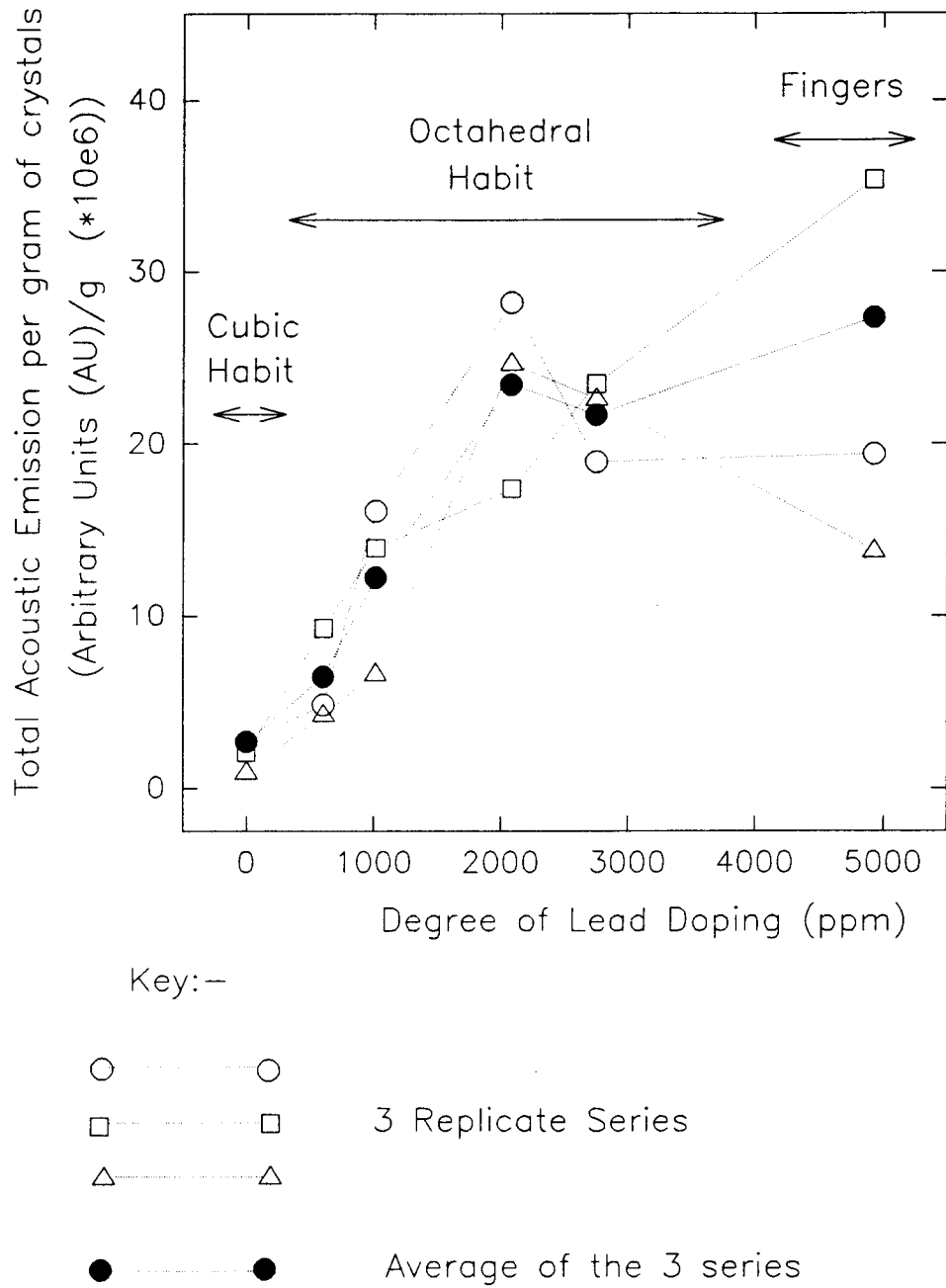


Fig 12. Variation of total acoustic emission per gram of KBr crystals grown during preliminary study. Crystal morphology influenced by Pb doping.

repeated trial across the solutions of series #1. The sample size in the majority of cases was such that between 0.1-0.2 g of crystals were produced.

It was postulated that the trend in AE per gram of crystals grown (fig. 12) was due to the change in the KBr crystal morphology because of the influence of the lead dopant. A more comprehensive study of the effect of the crystal morphology grown on the AE observed was thus undertaken. The findings are reported in the following sections.

3.2 Comprehensive Morphological Study of KBr

A comprehensive study of the different growth morphologies of KBr doped with Pb and the associated acoustic emission produced was undertaken using the solutions of series #2 and series #3.

Solutions of series #2 were used to compare the rate of acoustic emission and rate of image whitening for the different KBr morphologies grown. Solutions of series #3 that produced the same KBr morphologies as series #2 provided acoustic waveform data for crystal growth.

3.2.1 Crystallization Sequences at a Magnification of x20

As the solutions of series #2 were allowed to evaporate the KBr crystallized in distinct morphologies, which depended on the level of lead dopant within the evaporating solution. Scanning electron micrographs for 0-29000 ppm Pb dopant are shown in figs. 13, 14, 15. The total mass of crystals grown was between 0.06-0.12 g for the experiments carried out.

The following crystallization sequences were observed. With 0 ppm Pb doping, individual cubes of KBr were seen to nucleate and grow within the drop (fig. 13a), until eventually when almost all the solution had evaporated the individual cubes began to touch, and grow together. No acoustic emission accompanied the nucleation and growth of the solitary KBr cubes. However, acoustic signals were observed as soon as the cubes began to touch and grow into each other. This can be clearly seen in fig. 16a where the acoustic integration trace and the image whitening curve are offset in time, with the acoustic integration lagging behind the image whitening. In fact the majority of the acoustic emission was observed after the crystals had visually "stopped growing". For a discussion of the source of this acoustic emission see section 3.3.

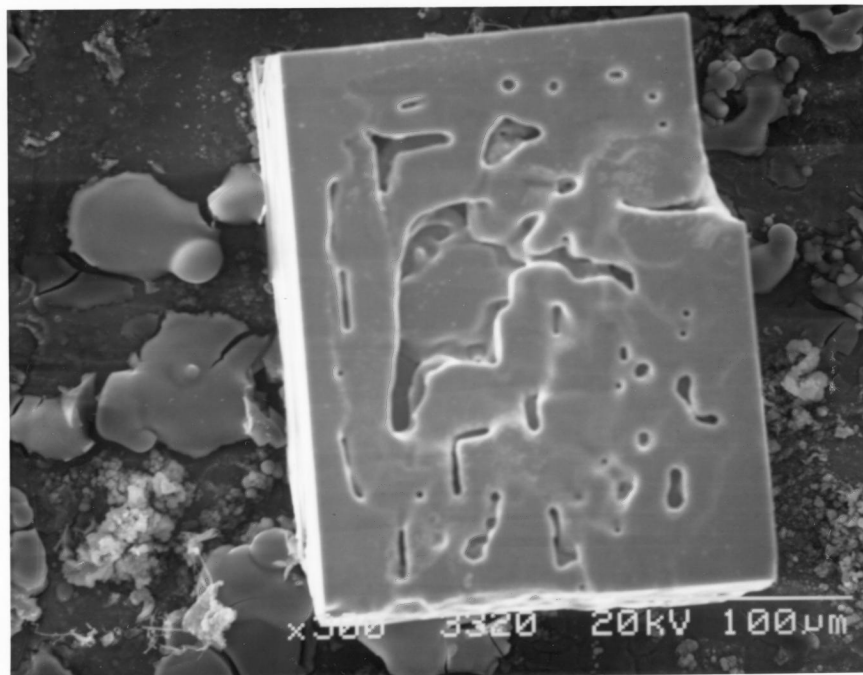
As the dopant level of Pb increased from 0 to 1990 ppm the KBr crystal habit changed from cubic to octahedral (fig. 13b). The crystals showed increased tendency to clump together during the initial nucleation and growth phases, so that groups of two or three crystals were observed together. The acoustic integration trace showed a distinctive two stage rise (fig. 16b), with the first stage following the image whitening exactly. The second rise, which occurred after the image whitening had maximized, indicated again that much emission comes after the crystals had "stopped growing", as was seen with the solutions at 0 ppm Pb dopant.

At dopant levels of between 1990-4080 ppm Pb the KBr crystals were all octahedral, and began to cluster even more during the initial stages of evaporation, with groups of four or more tiny octahedra growing together (fig. 14a). This is the beginning of the growth of the dendritic form of KBr. At 4080 ppm Pb the acoustic integration trace very closely paralleled the image whitening (fig. 16c), without the second rise seen in fig. 16b for crystals grown with 1990 ppm Pb dopant. Less acoustic emission is now seen after the maximum image whiteness has been reached. A decrease in the size of the

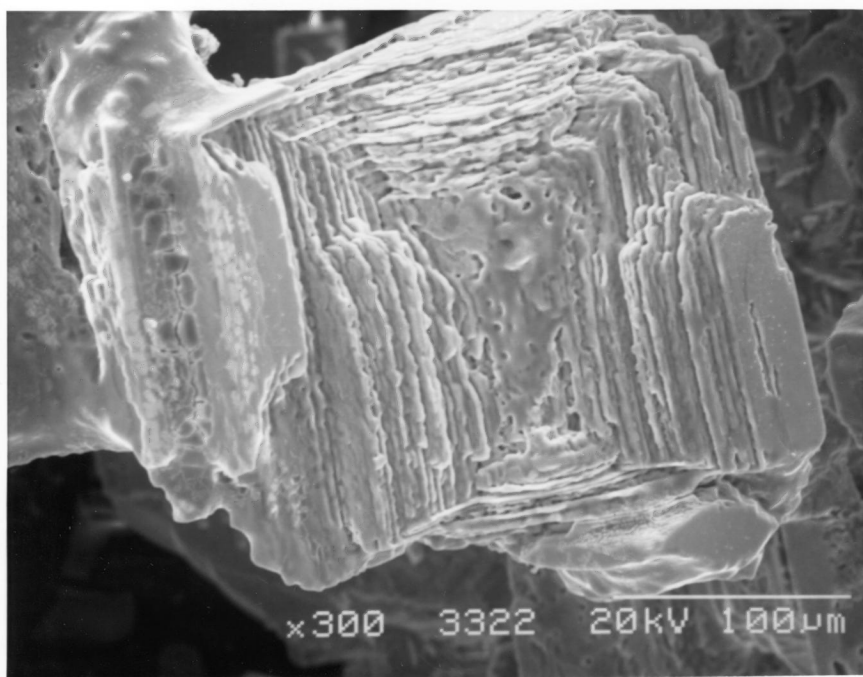
octahedra is seen at dopant levels of between 1990–4080 ppm when compared with those produced at dopant levels of between 0–1990 ppm (see figs. 13b, 14a).

At dopant levels of between 4080–8020 ppm Pb, fingers of KBr [60] were seen to grow outwards from the edge of the drop, with islands of crystals observed in the centre of the droplet. Less spreading of the finger-like growth of KBr from the boundaries of the droplet was observed compared with the preliminary experiments. This was due to the smaller droplet size used (100 μ l instead of up to 250 μ l). The growing "fingers" were thus able to be kept within the field of view of the microscope. Microscopic analysis of these KBr fingers by SEM showed that they were comprised of long chains of many tiny coupled octahedra 25 μ m or less in size (fig. 14b), while the central islands were found to be clusters consisting of up to 10 tiny octahedra of similar dimensions. These tiny octahedra were smaller than those observed in the dopant range of 1990–4080 ppm. This dendritic form of KBr gave excellent agreement between the acoustic integration and the image whitening traces, and little or no acoustic emission was observed after the crystals stopped growing (figs. 17a).

At dopant levels of 12210 ppm Pb and above, needle crystals were observed within an octahedral matrix (figs. 15a, 15b) that consisted of a mat of many octahedra of varying sizes. These octahedra were larger than those produced during the growth of the dendritic form of KBr. This mat grew with much interaction of the crystals unlike the individual crystal growth seen for the cubic form. Good agreement between the image whitening trace and the acoustic integration trace start and finish times was observed, but in 10 of 21 cases with lead dopant above 12210 ppm some emission was observed after the maximum image whiteness was reached. This is indicated by the second acoustic rise in fig. 16d which occurred about one hour after the crystals had visibly "stopped" growing.



(a)



(b)

Fig 13. Scanning electron micrographs of (a) cubic KBr at 0 ppm Pb dopant, and (b) cubic to octahedral change of KBr at 1990 ppm Pb dopant.

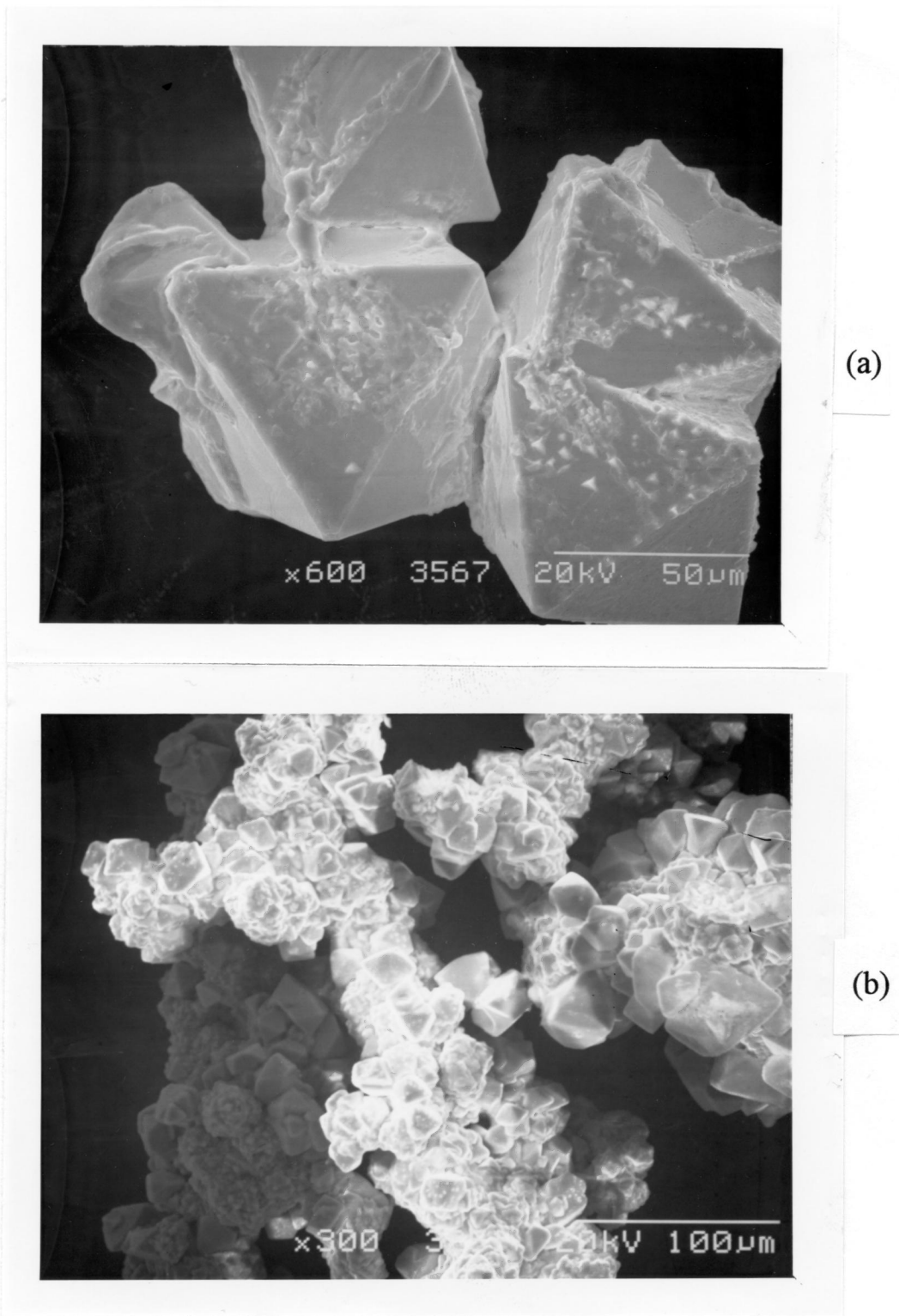
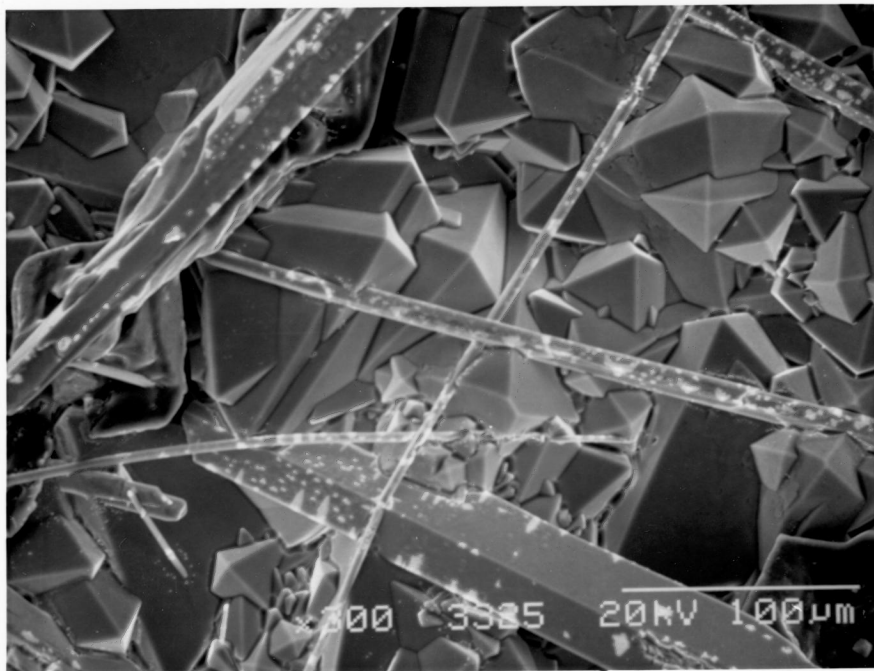
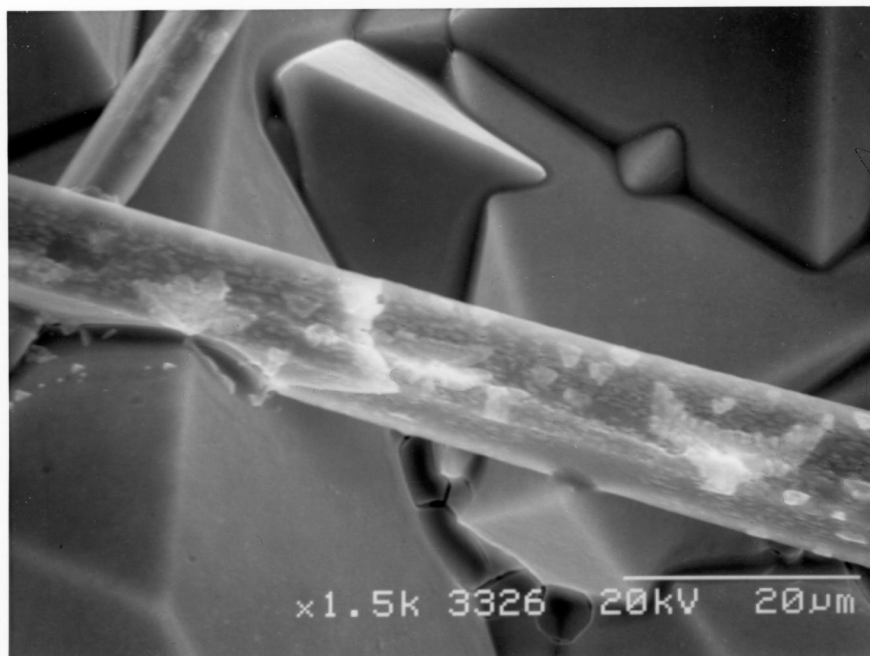


Fig 14. Scanning electron micrographs of (a) central islands of KBr observed in droplet at 4080 ppm Pb dopant, showing the clustering of the octahedra, and (b) dendritic fingers of KBr at 6070 ppm Pb dopant.



(a)



(b)

Fig 15. Scanning electron micrographs of (a) K₂PbBr₄ needles in an octahedral matrix of KBr, observed at 24840 ppm Pb dopant, and (b) enlargement of the central portion of fig. 15a, showing the interpenetration of a needle with the octahedral matrix.

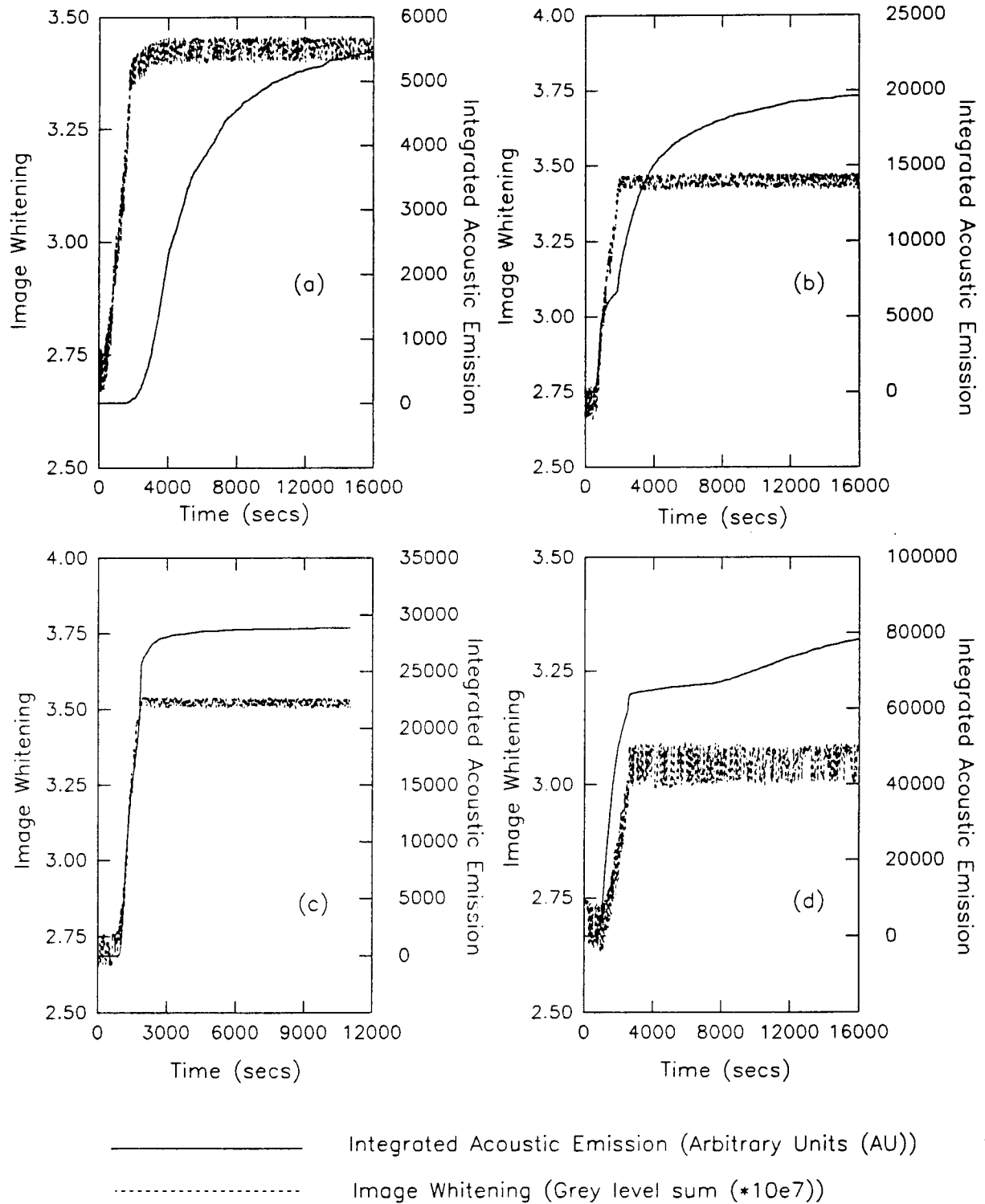


Fig 16. Integrated acoustic emission and image whitening curves with time, for the growth of KBr crystals viewed at a x20 magnification with varying amounts of lead dopant, (a) 0 ppm Pb, (b) 1990 ppm Pb, (c) 4080 ppm Pb, and (d) 22060 ppm Pb.

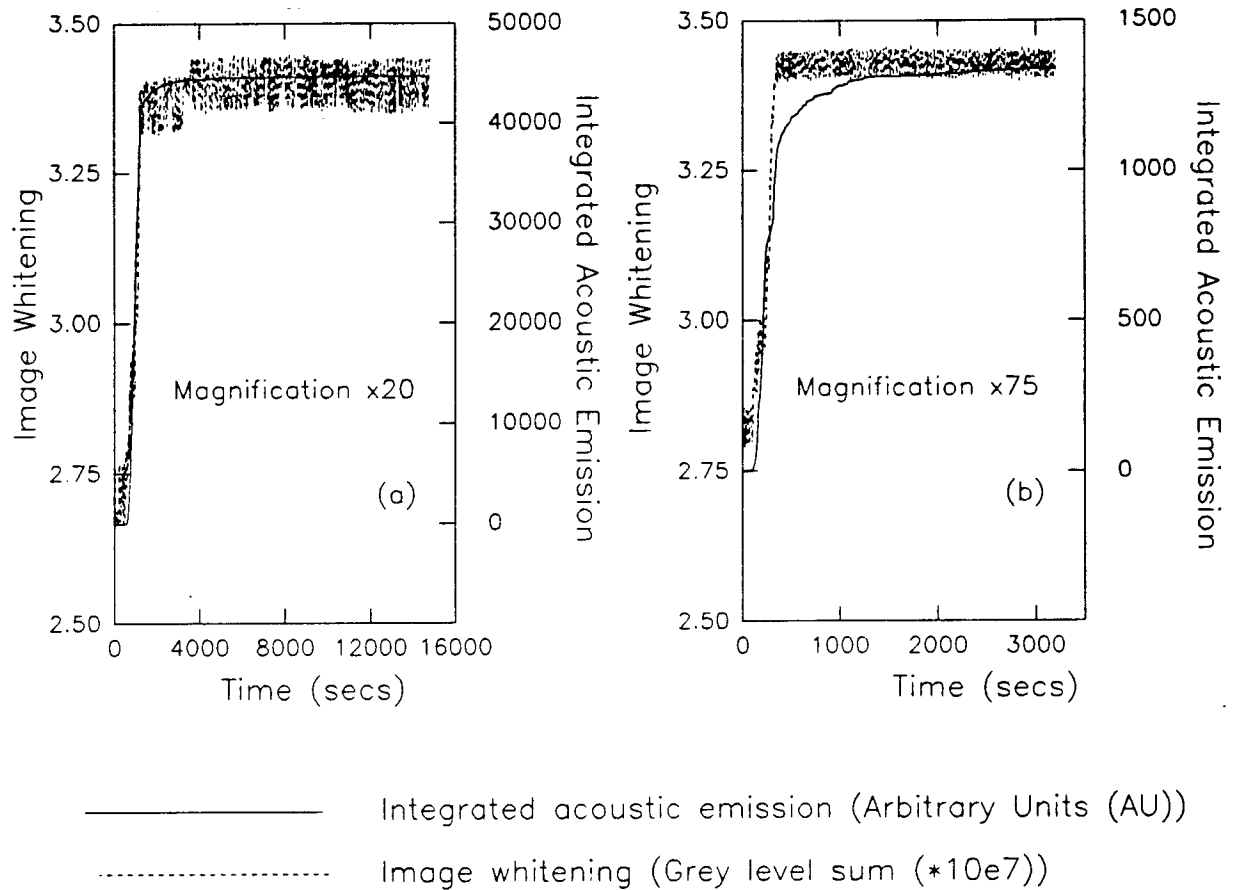


Fig 17. Integrated acoustic emission and image whitening curves with time, for the growth of the dendritic form of KBr crystals with 8120 ppm Pb. Two different magnifications shown, (a) x20, and (b) x75.

3.2.2 Studies at Magnification x75

Studies of all the different morphologies grown were also carried out at x75 magnification. The same trends were observed between the acoustic integration trace and the image whitening curves for all the morphologies. This included excellent agreement again for the dendritic form of KBr (4080-8020 ppm) described in the preceding section, where the acoustic integration trace was found to parallel the image whitening trace almost exactly (fig 17b). This is even more impressive when one considers that an exceptionally small mass of crystals grown was grown when using this magnification so as to keep all the growing crystals within the field of view of the microscope. The droplet size used for these increased magnification experiments was 4 μl which produced a mass of crystals on the order of 0.004 g.

Total acoustic emission per gram of crystal produced was not calculated for the studies carried out at increased magnification due to the exceptionally small mass of crystals grown.

3.2.3 EDX and XRD analysis of Needles

The needles observed at dopant levels of 12210 ppm and above were identified by EDX analysis and XRD as K_2PbBr_4 . When analyzed by EDX the needles showed a large weight percentage of lead, 32%, relative to the octahedral matrix for which no lead was detected (table II and III). This amount of lead was consistent with the formula K_2PbBr_4 . However, given the roughness of the sample (non-ideal, in terms of the geometric assumptions made for truly quantitative EDX analysis), the EDX analysis was purely used as an indicator of the relative amounts of each element in the different growth forms observed, and not as a method of stoichiometric identification.

Table II.

Average values of weight and atomic percentages of K, Br, and Pb determined by Energy Dispersive X-ray (EDX) analysis for 3 different needles shown in fig. 15a. Theoretical values for K_2PbBr_4 are given for comparison. The range of experimental values was within $\pm 10\%$ (absolute).

Element	Experimental		Theoretical	
	Weight % (± 10)	Atomic % (± 10)	Weight %	Atomic %
K	16	34	12.92	28.57
Br	52	53	52.83	57.14
Pb	32	13	34.24	14.29

Table III.

Average values of weight and atomic percentages of K, Br, and Pb determined by Energy Dispersive X-ray analysis (EDX) at three different positions in the octahedral matrix shown in fig. 15a. Theoretical values for an octahedral crystal of KBr containing 29790 ppm are given for comparison. The range of experimental values was within $\pm 10\%$ (absolute).

Element	Experimental		Theoretical	
	Weight % (± 10)	Atomic % (± 10)	Weight %	Atomic %
K	37	54	29.65	48.51
Br	63	46	60.60	48.51
Pb	0	0	9.60	2.98

Table II does indicate though a good agreement between the theoretical atomic and weight percentages of K, Br, and Pb in K_2PbBr_4 and those observed in the 3 needle crystals grown at 29790 ppm Pb dopant. Table III showed that no lead was detected by EDX analysis in the octahedral matrix, whereas one might expect evenly distributed lead at a level of 29790 ppm to be detected. However, given that much lead is present as K_2PbBr_4 needles, the actual lead content of the octahedral matrix must have been significantly reduced. This is in keeping with the results observed.

A number of these needles (≈ 20) were collected by hand using tweezers and a magnifying glass, and ground to a fine homogeneous powder using pestle and mortar. Powder X-ray diffraction patterns were then obtained and compared with reference spectra for KBr, K_2PbBr_4 , $KPbBr_3$, and KPb_2Br_5 . The best spectral match was found to be from K_2PbBr_4 (table IV, fig. 18).

The crystal structure and lattice parameters of $K_2PbBr_4 \cdot H_2O$ have been reported previously [66]. Comparison of the experimentally obtained XRD pattern with standard patterns from the International Centre for Diffraction Data confirmed the stoichiometry of the needles. The first two XRD peaks at positions of $2\theta = 12.4^\circ$ and 13.6° were the main diagnostic peaks used (see table IV). Two other possible stoichiometric combinations of K, Pb and Br exist, $KPbBr_3$ and KPb_2Br_5 . The XRD pattern for $KPbBr_3$ does not show any peaks below $2\theta=21.6^\circ$ however, and KPb_2Br_5 while having peaks at a similar position to K_2PbBr_4 also has a major peak at $2\theta=9.5^\circ$ and numerous peaks between $2\theta=13.5^\circ$ and 20° where the observed XRD pattern had none. Obviously, one would expect a little pure KBr from the octahedral matrix (fig. 15a) to be present as the needle separation was carried out manually. The XRD pattern observed (fig. 18a) showed a combination of peaks from KBr and K_2PbBr_4 , and thus did confirm the preliminary compositional analysis of the needles determined by EDX.

The white spots observed on the needles in figs. 15a, 15b were examined for compositional variation with respect to the bulk needle by EDX. No compositional difference was found. It is possible that the white spots are evidence of internal damage of these needles. There is some evidence for this as most of the white spots occur along the edges of the needles and at points of interaction with the octahedral mat.

Table IV.

Powder X-ray diffraction (XRD) peak positions for K_2PbBr_4 and KBr obtained from the International Centre for Diffraction Data, Powder Diffraction File #2. Compare with fig. 18.

Peak Positions of K_2PbBr_4 2 θ (degrees)	Peak Positions of KBr 2 θ (degrees)
12.422	23.331
13.633	26.983
19.936	38.528
21.188	45.521
21.821	47.684
22.262	55.663
23.580	61.140
24.164	62.922
25.353	69.737
26.427	74.636
27.593	82.626
27.768	87.336
29.063	88.909
29.817	95.142
32.209	99.872
34.208	101.431
34.701	107.902
34.967	112.901
35.409	114.597
35.847	121.696
38.185	127.380
39.892	138.037
40.359	148.467
41.625	
44.834	

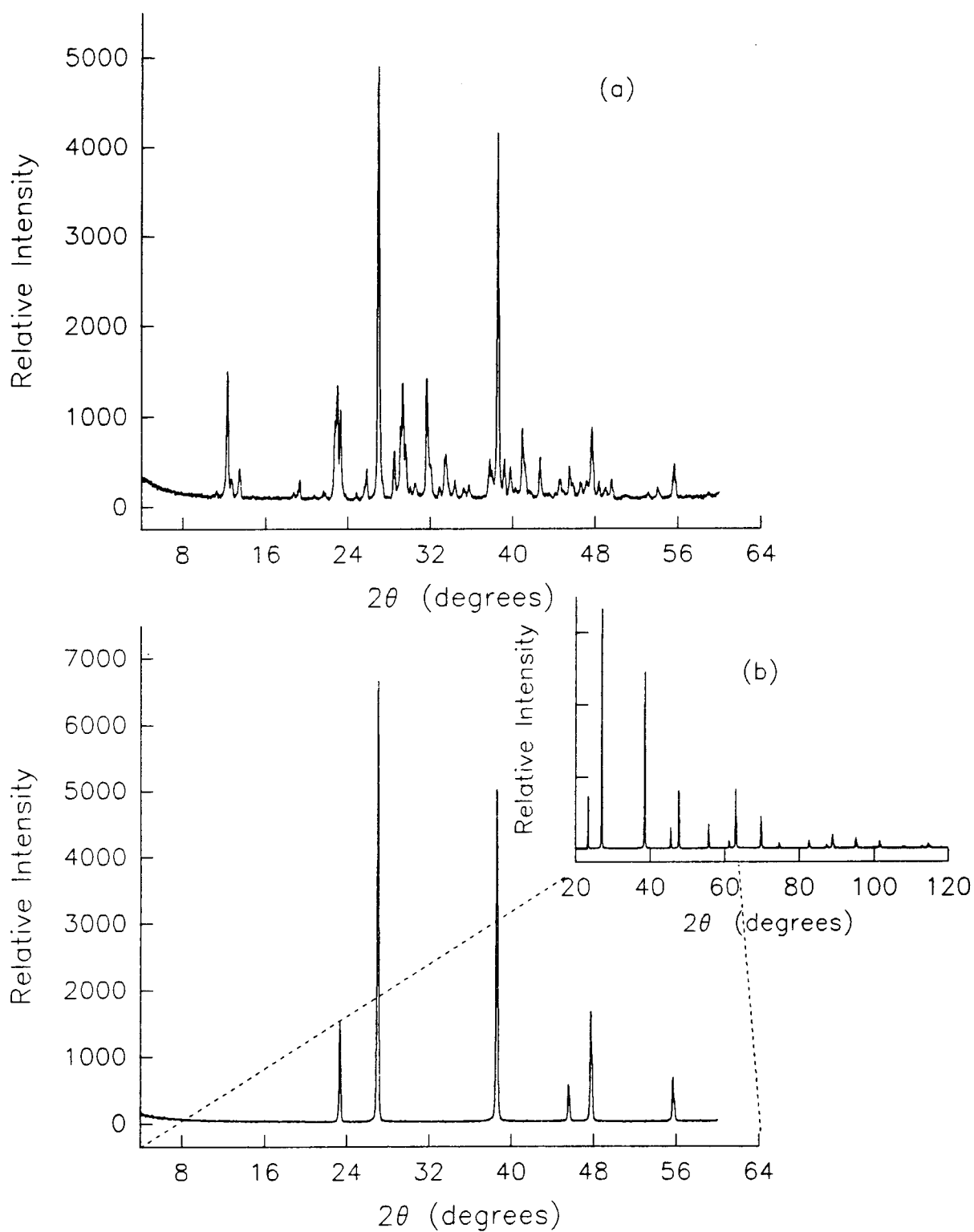


Fig 18. Powder X-Ray diffraction patterns for (a) needle crystals collected during the growth of KBr crystals from a solution doped with 29790 ppm Pb, and (b) analytical grade KBr.

3.2.4 Trends in Integrated Acoustic Emission

The total acoustic emission was recorded for each replicate of the different KBr morphologies and normalised to the mass of crystals produced ($< 0.12\text{g}$). The plot in fig. 19 shows the total acoustic emission variation with the degree of lead doping due to the changes in morphology of the KBr crystals. A large increase (10 fold) in total emission can be seen as the level of lead dopant is increased from 0 ppm to 8020 ppm. Thereafter the total emission remains high, but is variable. The range of the results is such that the unequivocal confirmation of a second maximum at 24840 ppm Pb dopant was not possible (see fig. 19).

The lower variability in the total acoustic emission observed for the replicates of series #2 compared with series #1 is attributed to the difference in sample size. The larger sample size used for series #1 produced a greater spreading of the crystals outwards from the piezoelectric crystal sensor. The sensitivity of the transducer decreases with distance from the central piezoelectric crystal sensor and so some signals may no longer be observed. This limitation was confirmed during the course of the impact experiments (section 2.3.3.3).

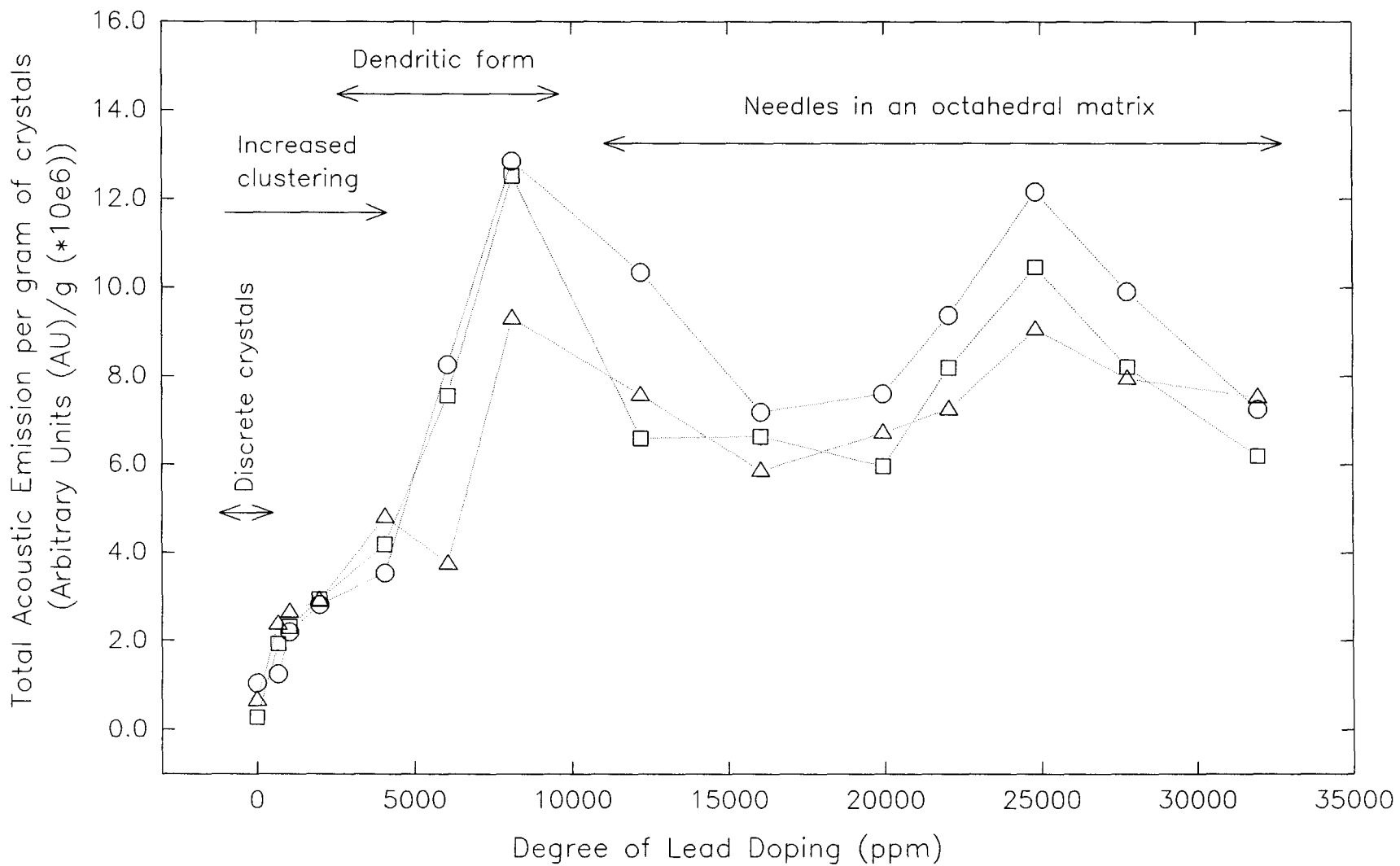


Fig 19. Total acoustic emission per gram of KBr crystals grown with varying amounts of lead dopant. 3 experimental series are shown.

3.3 Source of the Acoustic Emission

The proposed mechanism for acoustic emission generation during the crystallization of the different KBr morphologies is one of *inter-crystal interaction*. This is the first time such a mechanism has been postulated, and evidence for it will be discussed in the following sections.

3.3.1 Comparison of the Rate of Acoustic Emission to the Rate of Crystallization

Two different stages of acoustic emission activity occur during the recrystallization of potassium bromide, corresponding to two distinct rises in the acoustic integration profile. Firstly, there is the acoustic activity which for certain KBr morphologies paralleled the image whitening curve exactly, as in the case for KBr crystals grown with 8020 ppm Pb dopant (see fig. 17a, 17b). Then there is the acoustic activity which was observed after the crystals have visually stopped growing, such as in the case for the KBr crystals grown with 0 ppm lead dopant (see fig. 16a). In between these two dopant levels there are a series of two stage curves (see fig. 20), with the first stage following the image whitening curve exactly and then a second stage of activity seen after the crystals have stopped visually growing. As the dopant level increased from 0 ppm to 8020 ppm the second stage acoustic emission rise decreased until eventually at dopant levels above 4080 ppm Pb it disappeared completely, and only the first stage acoustic curve was evident. A second stage acoustic rise reappeared at dopant levels of 12210 ppm and above in 10 of 21 cases. This second stage acoustic rise again came after the maximum image whiteness had been reached.

The integrated acoustic emission profile evolution during the growth of KBr crystals with varying levels of lead dopant is shown in fig. 20. The first stage acoustic rise

closely paralleled the image whitening curves (figs. 15b, 15c, 16a, 16b). The evolution of this first stage acoustic rise can be seen across figs. 20a-20g. This evolution corresponded to the increased clustering observed for the KBr morphologies with increasing Pb dopant, until the dendritic form of KBr (which consisted of contiguous chains of tiny octahedra) was formed at dopant levels of between 4080-8020 ppm (fig. 20). The integrated acoustic emission profiles of the dendritic form of KBr shown in fig. 20 gave the best agreement with the image whitening curves. No acoustic emission was observed after the maximum image whiteness was reached for these forms (figs. 16c, 17a, 17b).

The acoustic emission activity which was seen to accompany the growth of the KBr morphologies between 4080-8020 ppm gave a reliable indication of the rate of growth of this particular morphology. Simultaneous acoustic emission with image whitening only appeared when the growth forms were such that many microcrystals nucleated and grew together (see figs 14a, 14b, 15a-octahedral mat), so that much *inter-microcrystal interaction* could occur.

Consider the solution in contact with the surface of the finger-like KBr structures produced with between 4080-8020 ppm Pb. As it evaporates, any tiny octahedral microcrystal that nucleates would exert a force on the neighbouring microcrystals within the structure. The force exerted by each microcrystal causes tiny cracks to develop in the bulk structure of the finger, leading to acoustic emission. Since many tiny microcrystals make up these structures, numerous potential sources of acoustic emission exist. Therefore for crystal morphologies consisting of these clusters of tiny microcrystals acoustic emission provides a very reliable method of monitoring the overall growth rate of the structure. The growth of the dendritic form of KBr which was observed between 4080-8020 ppm is perhaps the best evidence for the *inter-crystal interaction mechanism*.

The greatest number of possible acoustic sources for the inter-crystal interaction mechanism are present within the structure of dendritic KBr. This would account for the increase in the total amount of emission seen in fig. 19 over the dopant level range of 0-8020 ppm. The initial increase seen to occur between 0-4080 ppm could be accounted for by the increased clustering observed, before eventually leading to the dendritic form.

It is postulated that the acoustic activity which was observed after the crystals had stopped growing was in part due to the release of stresses which had developed as the crystals pushed against each other during their growth. This is primarily thought to occur by the movement of dislocations within the crystals and microcracking in and between crystals. Consider the small spaces between two cubic crystals. As they begin to touch any crystalline material that nucleates and grows between the two cubic crystals is going to induce some stress in the matrix, and thus provide a potential site for acoustic emission. The acoustic emission after the crystals had stopped growing is indicated by the second stage rise in the integrated acoustic emission profiles of fig. 20. It should be noted that the integrated acoustic emission profile for the undoped (0 ppm Pb) KBr (figs. 16a, 20) is a single stage curve. However, this curve consists entirely of what has been termed here the second stage acoustic rise, *i.e.* acoustic emission that occurred after the maximum image whiteness had been reached (see fig. 16a).

The plateauing seen in fig. 19 for those crystals grown with dopant levels greater than 12210 ppm can be explained by considering the size and number of octahedra which are present in the mat. The octahedral mat of these systems does not have as many inter-crystal interactions as the dendritic growth form observed at 8020 ppm due to the larger size of the octahedral crystals in the mat (100 μm) compared with those observed in the fingers of KBr at 8020 ppm Pb (<25 μm). There are thus less potential sites for the generation of acoustic emission. The numerical values for the total acoustic emission per

gram had a great variation for dopant levels of 12210 ppm and higher. This variation was attributed the growth and fracture of needles of K_2PbBr_4 (see section 3.3.4).

3.3.2 Integrated Acoustic Emission and Image Whitening Rise Times

A comparison of the rise times for both the integrated AE profiles and the image whitening curves for all levels of Pb dopant is illustrated in fig. 21. As can be seen the image whitening rise time is very similar across all levels of Pb dopant. This suggests that the relative saturations of the starting solutions and the ambient conditions in the laboratory were such that the rates of crystal growth were similar for all solutions studied. This is important as the speed of the many physical phenomena has a direct bearing on the amount and rate of acoustic emission generated [10].

The rise times were calculated by considering the time taken for the curves to rise from 10% to 90% of the final value. The agreement between the average total AE rise time and the average image whitening rise time (at one dopant level) increased as the dopant was increased from 0-8020 ppm. Beyond this point it showed a greater degree of variability. The best agreement between the rise time of the two profiles is observed for the dopant range of 4080-8020 ppm where the greatest clustering of micro-crystals is observed. This is as expected from figs. 14a, 14b. The AE rise time for the signals collected during the growth of KBr crystals with 0 ppm dopant is much larger than the image whitening rise time. This showed that much acoustic emission occurred after the crystals had visually stopped growing. The variation between the average total AE rise time and the average image whitening rise time at dopant levels above 12210 ppm was due to the second stage rise (see figs. 16d, 20). When one considers just the average AE rise time for the first stage acoustic rise only, then the agreement with the average image whitening rise time at dopant levels of 12210 ppm and above is excellent (see fig. 21).

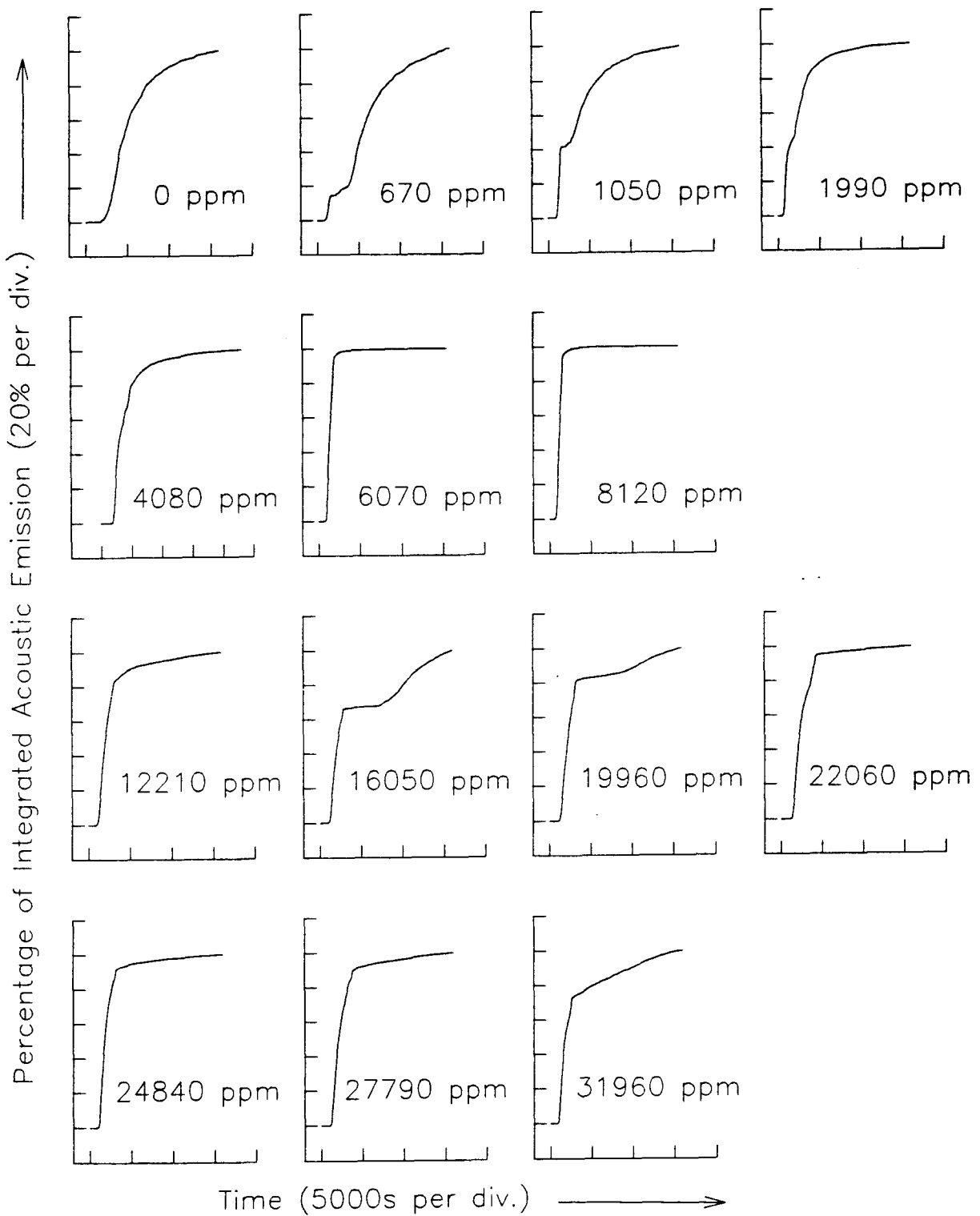


Fig 20. Integrated acoustic emission profiles observed during the growth of KBr crystals with varying degrees of lead dopant.

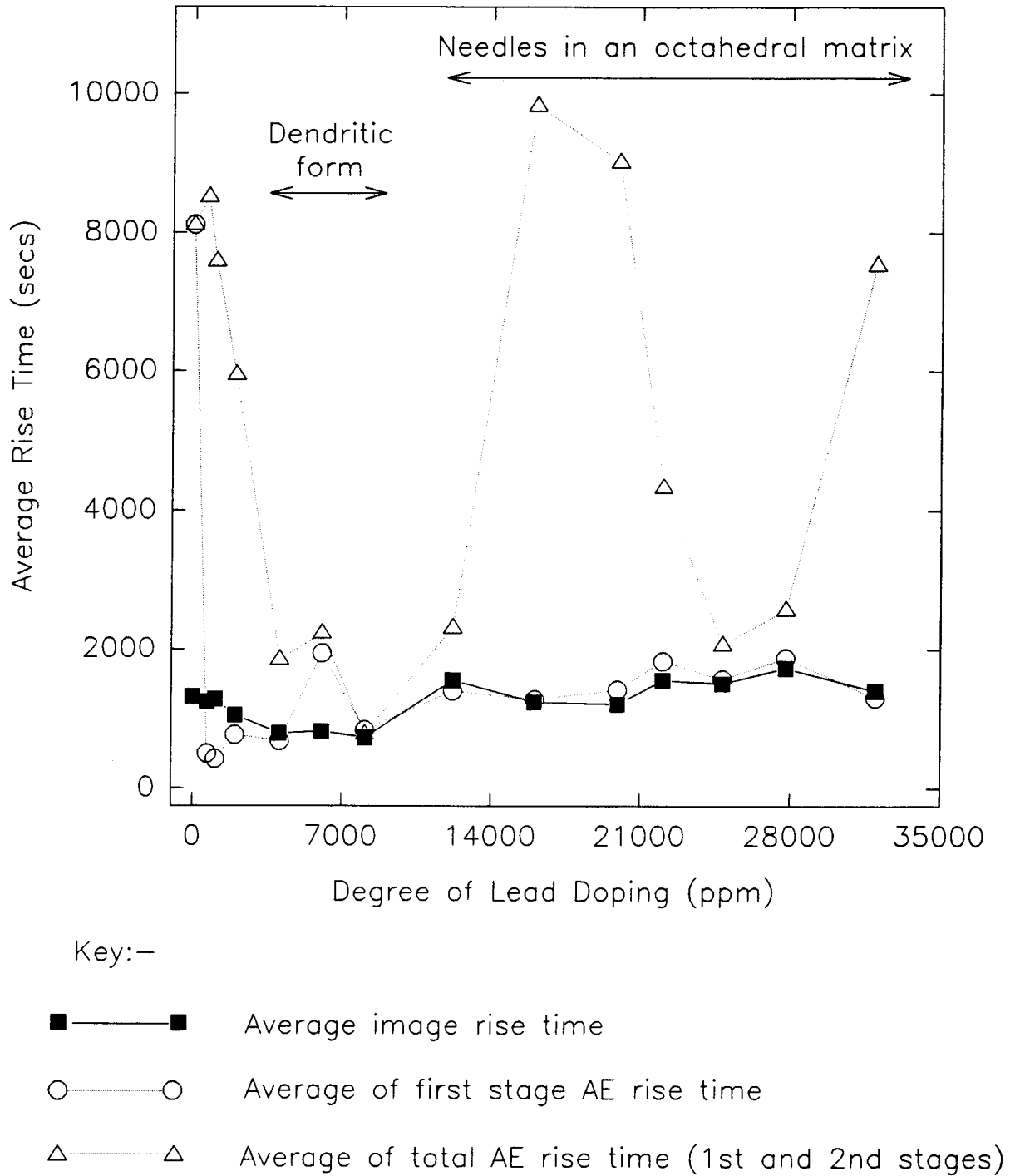


Fig 21. Comparison of acoustic integration and image whitening rise times as the KBr crystal morphology is changed by increasing the lead dopant.

3.3.3 Dimensionality of the Dendritic Growth Form

The dendritic growth form of KBr occurring between 4080-8020 ppm was observed to grow outwards from the solution droplet to cover the surface of the transducer. The "dendrites" produced were irregularly shaped and twisted in all directions with further branchings on each outgrowth observed. These finger-like structures were observed in most cases to rise from the surface of the transducer by as much as 1 cm to produce a tree-like structure in 3 dimensions (fig. 11). Occasionally however, the growth observed was confined to 2 dimensions on the surface of the transducer. These fingers were observed to be much thinner (less clustering) and spread further.

A comparison of the two forms showed that the total emission of the 2D growth was lower (reduced by half or more) per mass of crystal than the 3D form (see fig 22). This result can be rationalised by considering the inter-crystal interaction mechanism proposed earlier. During the growth of the 2D form one degree of interaction has been removed, and indeed the fingers observed were thinner due to less clustering of the microcrystals in the structure. Again this result is in keeping with the proposed mechanism.

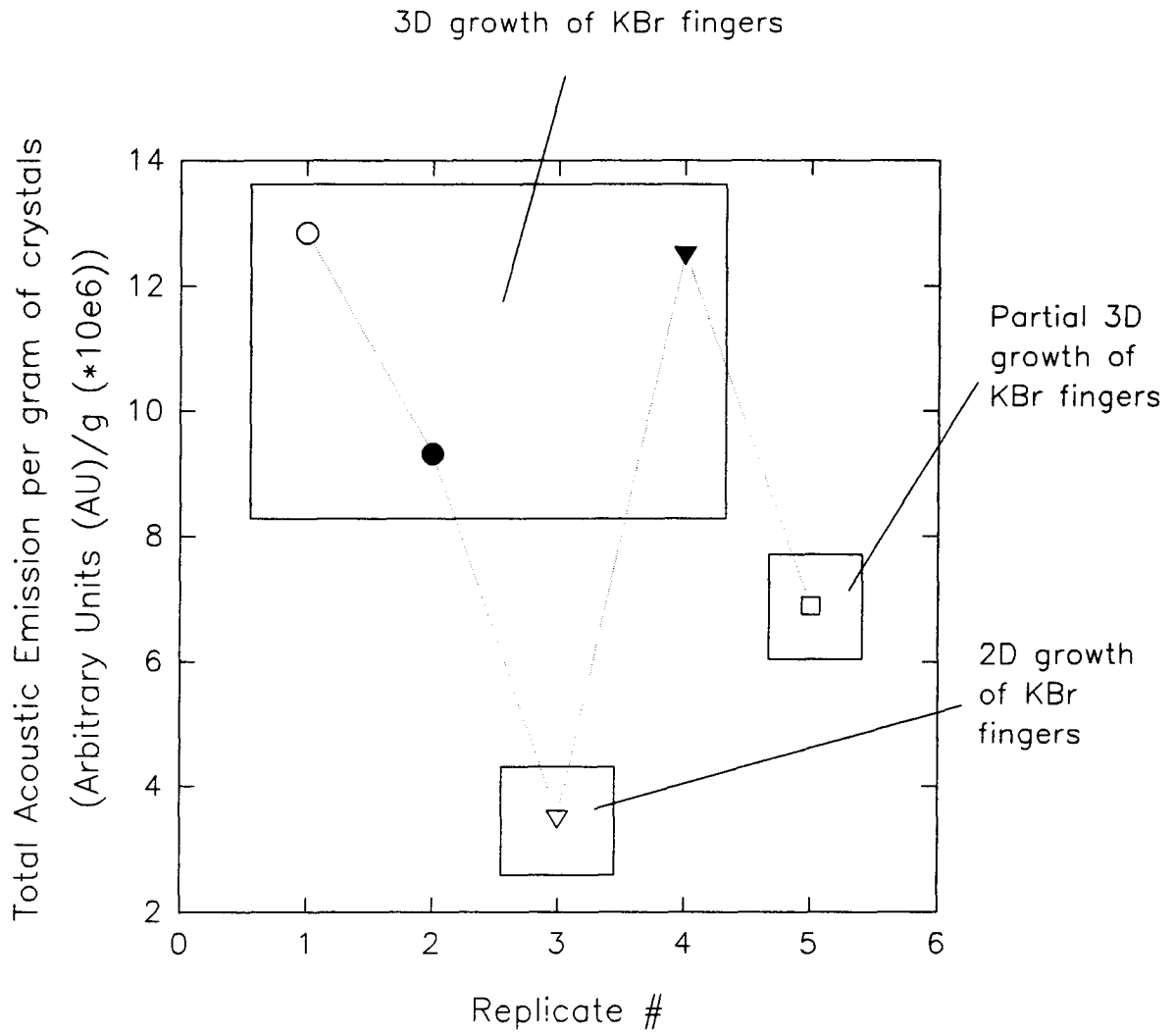


Fig 22. Total acoustic emission per gram of crystals produced during the growth of 5 replicate samples of KBr doped with 8120 ppm Pb.

It was postulated that the change in dimensionality observed for this growth form was related to the rate of evaporation of the droplet. The ambient temperature did not change significantly during these replicates, but on examining climatic data for the days on which the crystals were grown the relative humidity was found to have changed significantly. It was therefore appropriate to determine if a correlation existed. Meteorological data collected on an hourly basis were obtained from the University of British Columbia's Climate Station. The relative humidity (R.H.) measurements yielded the saturated water vapour pressure of the air by using Tetens' empirical formula (1). The relative humidity relationship (2) was then used to calculate the actual water vapour pressure at any hour:

$$e' = (0.6108) \text{ antilog}_{10} [7.5 T / (T + 237.3)] \quad (1)$$

$$\text{R.H.} = 100 e / e' \quad (2)$$

where e' = saturation vapour pressure (kPa), e = vapour pressure (kPa) and T = temperature ($^{\circ}\text{C}$).

Given that the chemistry department is vented directly to atmosphere with no artificial methods of humidification it might be expected that the meteorological vapour pressure trend would approximate that inside the laboratory. A comparison of the total acoustic emission per gram of crystals grown with the initial vapour pressure showed no trend (see fig 23). The 5 replicate experiments considered produced both 2D and 3D dendritic forms of KBr (8020 ppm Pb). Indeed no trend was observed between the vapour pressure and total AE across the replicates of any of the KBr morphologies grown. These comparisons were made subsequent to completion of the crystal growth experiments.

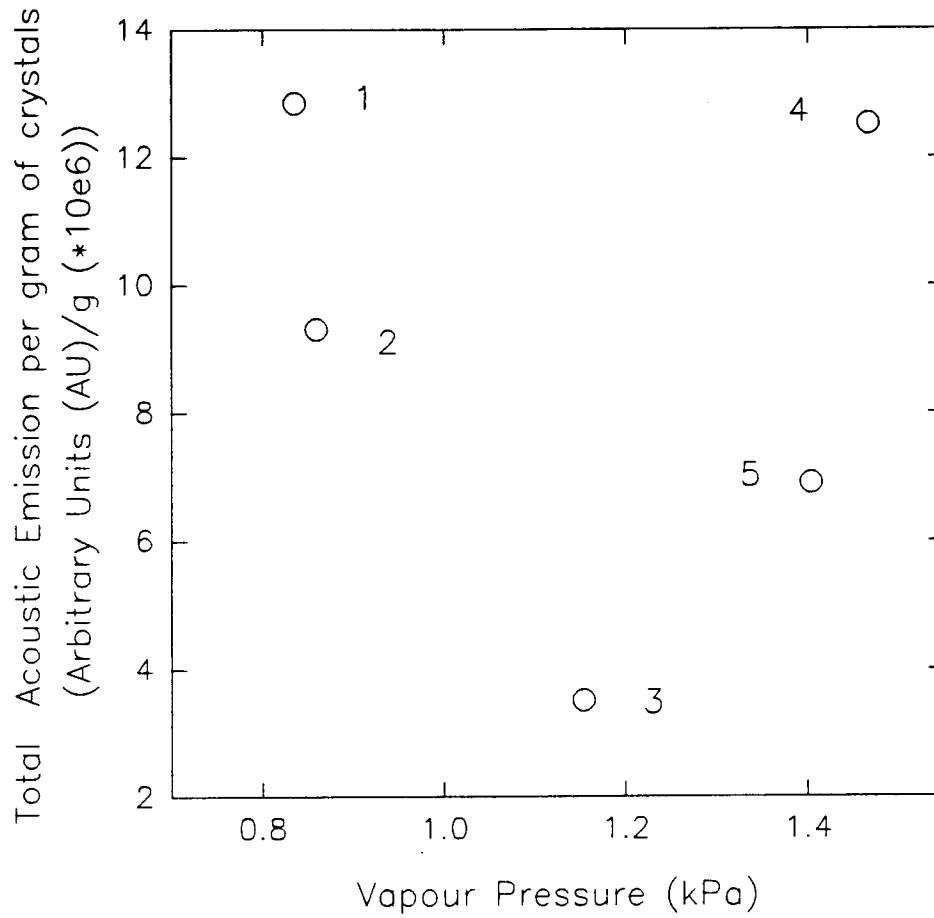


Fig 23. Effect of vapour pressure on the total acoustic emission per gram of crystals produced during the growth of the dendritic form of KBr with 8120 ppm Pb. Numbers 1–5 refer to replicates of fig. 22.

3.3.4 Fracture Related Damage at Dopant Levels Above 12000 ppm Pb

The needles observed at dopant levels of 12210 ppm and above grow into the edges of the octahedral crystals which form the mat. Fig. 15b shows such an interaction. There is damage at the point of contact between the needle and the octahedra, with associated debris at that location (LHS, fig. 15b). Complete fracture of these extremely fine needles may also occur. A close examination of fig. 15a indicates some misalignment of the needles where they encounter the edges of octahedra within the mat. The damage due to the interaction of the needles with the edges of the octahedra (flaking of debris) and the complete fracture of the needles, would be possible sources for acoustic emission. Fracture would be an exceptionally "loud" event (discussed below). Variation in the number of needle breakages would account for the larger degree of scatter in fig. 19, at dopant levels of 12210 ppm and above.

3.4 Characterization of Crystallization Processes by Acoustic Waveform Analysis

The signals collected were classified prior to being analyzed in both the time and frequency domain.

3.4.1 Generation of Different Signal Classes

Acoustic frequency data were collected for each different KBr morphology using a bandwidth of 1.25 MHz. Each individual signal was described by 32 mathematical descriptors (see table I). These descriptors, their mathematical meaning, and their interpretations have been fully described elsewhere [17, 67]. From the 1000's of signals collected for each KBr morphology a random (computer random number generator) sample set of 50 signals was selected. Signal sets collected during the growth of 6

different KBr morphologies were combined and classified to form a single set of 300 signals. The signals collected for the dendritic form of KBr at 5900 ppm Pb dopant and 7620 ppm Pb dopant were treated as one class (\square). Signals from the KBr morphologies observed at 24920 ppm Pb dopant, and 29790 ppm lead dopant were treated as a second class (Δ). Signals from the KBr morphologies observed at 0 ppm (\circ) and 15980 ppm (∇) were each treated as separate classes. The reduction in the number of signals, from the 1000's collected to 50 signals per class, decreased the computational time for subsequent PCA calculations. The resulting principal components plots also remained relatively uncluttered, enabling the different signal classes to be readily identified.

This set of 300 signals was then compared with the artificially generated signals designed to mimic secondary nucleation phenomena (see section 2.3.3.3)

3.4.2 Signal Intensities

Typical acoustic signals for these 6 classes were selected by comparing each signal's descriptor values with the average descriptor values for the class. The signal with the lowest variance (from the mean) for each data set, over all the descriptors used was thus selected as typical, so avoiding any bias. These signals and their power spectra are shown in fig. 24.

It should be noted that the intensity of all the signals is at least ten times larger than the background blank (compare with fig. 6). Further, that the intensity of the signal due to artificial fracture is much greater than that observed during the growth of the different KBr morphologies. The intensity of the signals observed during the growth of the dendritic form of KBr (at 4080-8020 ppm), a plural crystal, showed no intensity difference from those signals collected at 0 ppm Pb. This is contrary to what Sawada *et al* observed

during the precipitation of sodium thiosulphate when the production of plural crystals was accompanied by acoustic signals of the greatest intensity [6].

Although the artificially generated signals do not mimic the processes of secondary nucleation exactly, the large difference in intensity of the signals of bulk fracture (fig. 24d) compared with the signals observed during growth (figs. 24a-24c) has significant ramifications. AE is of interest for non-invasive monitoring of industrial crystallizers. Care would be needed if detection of growth signals were to be a desired analytical parameter, since it is likely that any growth signals will be below the background level set for any industrial monitoring.

The average power spectra (AVP) for the same processes indicated in fig. 24 are shown in fig. 25. The AVP's clearly demonstrate the similarity of the signals observed during the growth of the different KBr morphologies (figs. 25a-25c). It can also be clearly seen from fig. 25 that the AVP's observed during growth are much more akin to the artificial fracture signal (fig. 25d) than to the impact signal (fig. 25e).

It should further be noted, that during the bulk fracture of the dendritic fingers of KBr, any crack would propagate around the edges of all the small microcrystals. The power spectra of individual signals of this bulk fracture and the AVP calculated across all the signals of bulk fracture are thus almost identical (compare figs. 24d, 25d). The individual signals arising during the formation of the dendritic KBr morphology result from the microfracture around just one microcrystal. The resulting power spectrum of an individual signal in this case is much less complex than that produced during the bulk dendritic finger fracture (compare figs. 24b, 24d). The average power spectra of these two processes are however very similar (compare 25b, 25d). This is further evidence for the *inter-crystal interaction* mechanism.

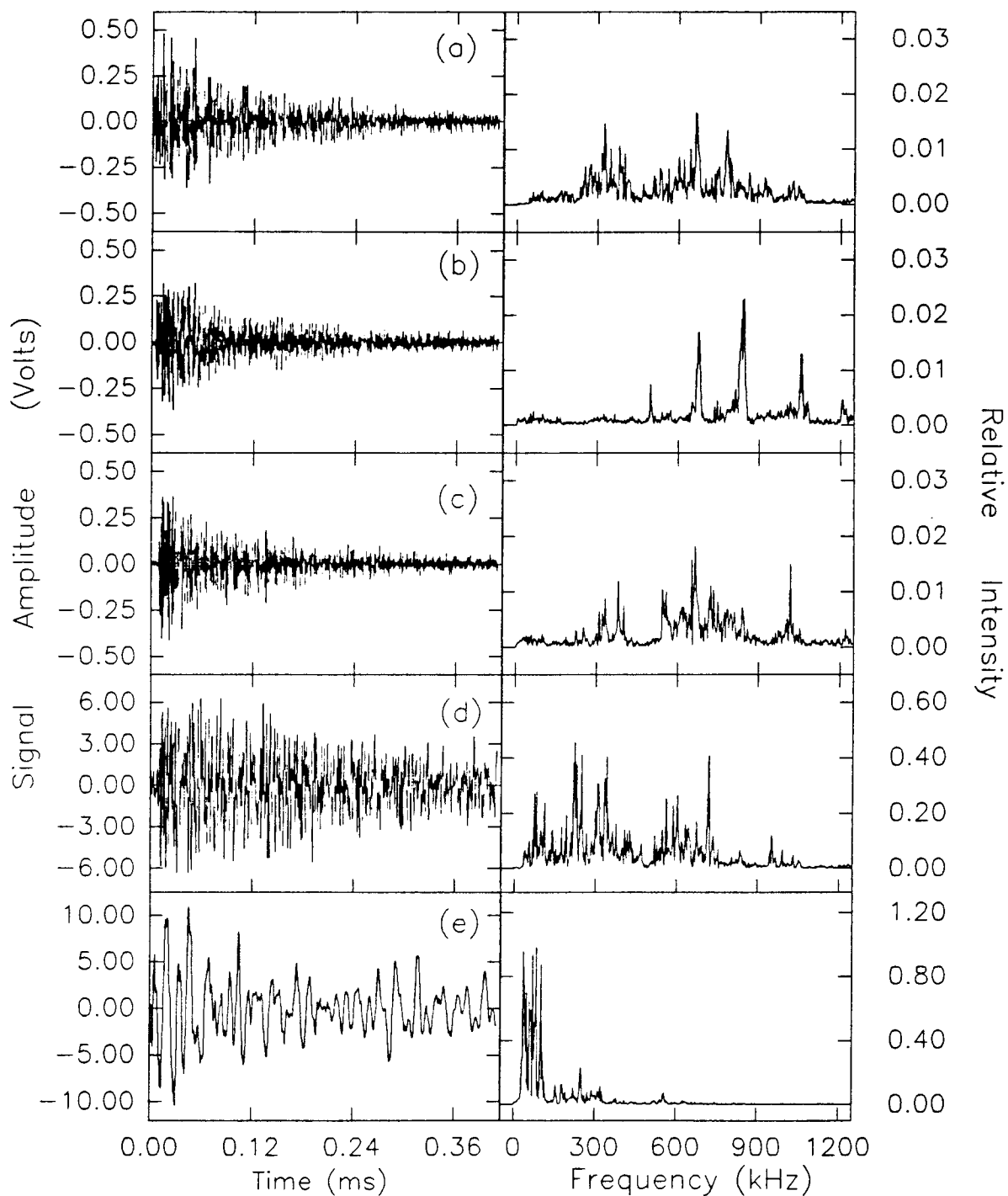


Fig 24. Typical acoustic signals and associated power spectra for KBr crystals grown with (a) 0 ppm, (b) 7620 ppm and (c) 24920 ppm Pb dopant, (d) bulk fracture of fingers of KBr grown with 7620 ppm Pb dopant, and (e) impact of KBr crystals on the transducer surface.

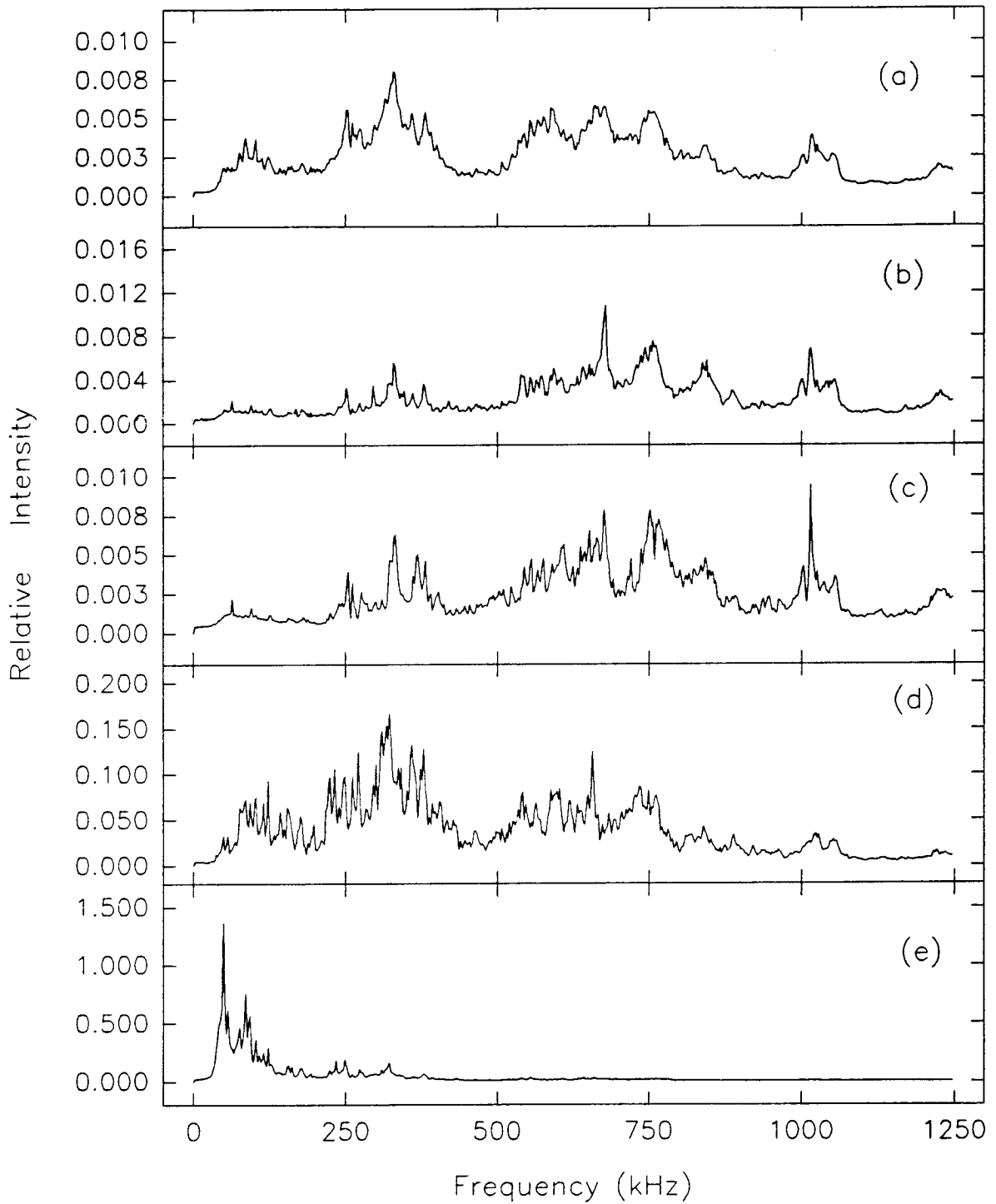


Fig 25. Average power spectra for acoustic signals collected during the growth of KBr crystals with (a) 0 ppm, (b) 7620 ppm, (c) 24920 ppm of Pb dopant, and artificially produced signals of (d) bulk KBr dendrite fracture, (e) KBr crystal impacts on the transducer.

3.4.3 Signal Class Separation by PCA

Principal Components Analysis (PCA) was used to ascertain if there were any differences in the acoustic signatures from the 6 different classes of acoustic crystallization signals. The number of descriptors used for PCA was reduced from 32 to 18 using the method outlined in section 2.4.2 (see table V).

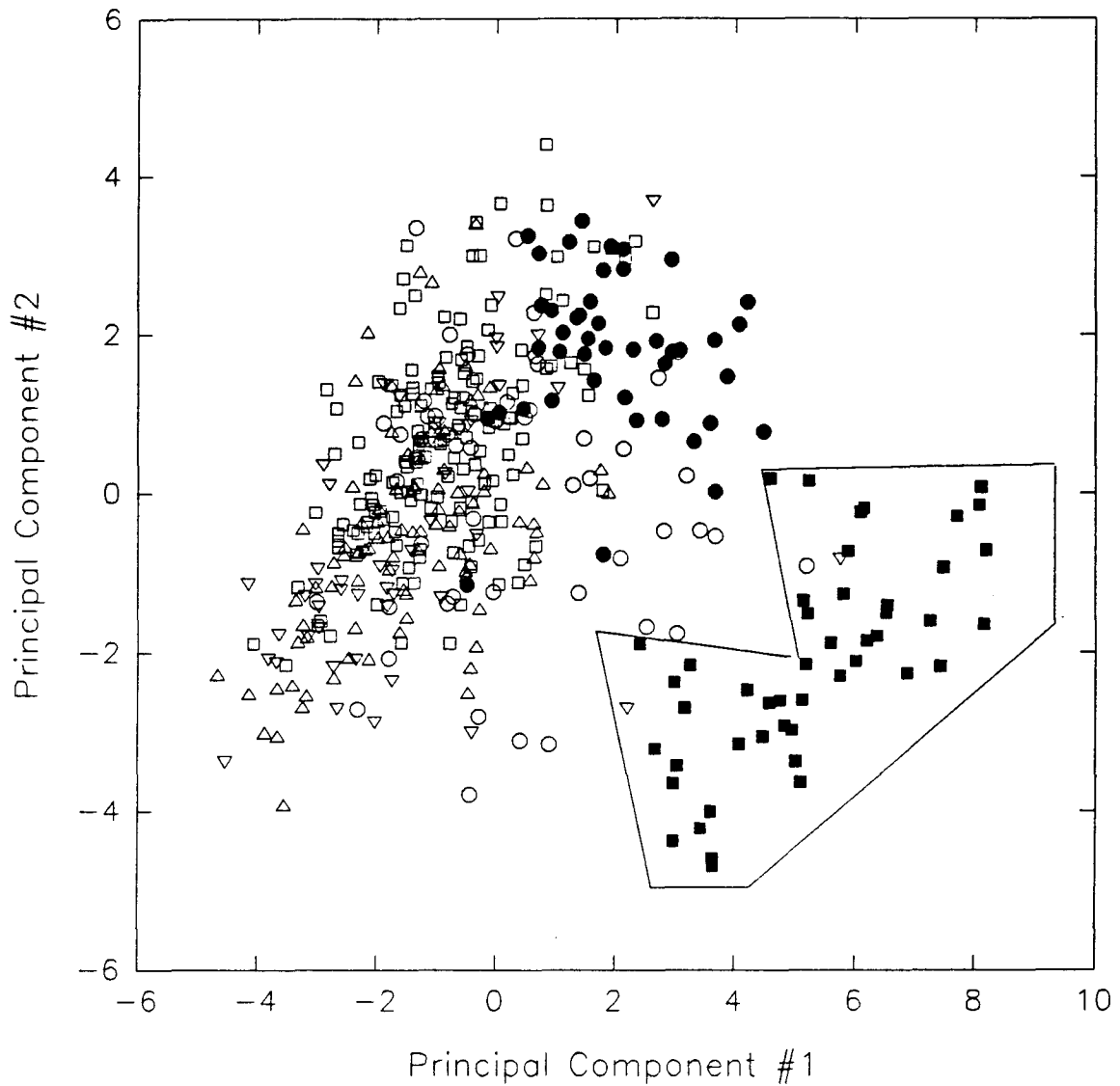
A plot of the first two principal components is shown in fig. 26. Two readily distinguishable sets of signals can be identified. One group consisted almost exclusively of acoustic signals generated by the impact of KBr crystals on the transducer surface (■); while the other group consisted of a tight cluster of acoustic signals from the crystal growth of the higher doped KBr crystal morphologies, (5900 and 7620 (□), 15980 (▽), 24920 and 29790 ppm Pb (Δ)), together with a secondary cluster of acoustic signals observed during the artificial fracture of KBr dendrites (●). The acoustic signals observed after the KBr crystals doped with 0 ppm Pb had stopped growing (○) were scattered throughout this second group, with the characteristics of some signals observed at 0 ppm Pb dopant being very similar to the impact signals that were artificially produced.

In order to obtain a better separation of the signal classes, the artificially produced signals of KBr dendrite fracture and impact were then compared with those signals generated during the growth of two distinctly different KBr morphologies, the dendritic form of KBr (5900 and 7620 ppm Pb), and the undoped cubic form of KBr (0 ppm Pb) again using PCA. These four classes of acoustic crystallization signals were then compared pair-wise.

Table V.

Descriptors that showed the highest resolution for the 6 different classes of crystallization signals.

Time Domain Descriptors	
RMS	Root mean square voltage
CREST	Ratio of peak voltage to root mean square voltage
KURTOSIS	4 th statistical moment (deviation from a Gaussian distribution)
T@AREA/2	Time to half area (signal decay measurement)
10-CROSS	Number of times signal crosses +/- 10% of maximum voltage
TIME OCTILES 1/8, 5/8, 8/8T	Normalized time octiles of root mean square voltage
Frequency Domain Descriptors	
FRQ@MAX	Frequency of highest intensity in the power spectrum
FRQ MEAN	Frequency equal to the summation of the intensity-weighted frequencies divided by the total intensity.
F-CREST	Ratio of the maximum power to the root mean square power
FBW>15%	Bandwidth of frequencies having intensities > 15% of maximum intensity
FQRTL BW	Bandwidth of frequencies between the second and third intensity integrated quartiles
FREQUENCY OCTILES DFB1, 2, 5, 6, 7	Normalized area in each power spectrum octile



Key:—

- | | |
|----------------------------------|--------------------------------|
| KBr crystal growth signals with: | Artificially produced signals: |
| ○ 0 ppm Pb dopant | ● KBr dendrite fracture |
| ▽ 15980 ppm Pb dopant | ■ KBr impact |
| △ 24920 and 29790 ppm Pb dopant | |
| □ 7620 and 5900 ppm Pb dopant | |

Fig 26. Principal components analysis showing the separation of different crystallization processes. Only 18 of 32 descriptors were used (see table V).

For each pair of classes selected the highly correlated (>90%) descriptors were again discarded, and the remaining descriptor differences between the two classes were analyzed. The three descriptors which showed the highest resolution for each pair were then used for PCA. The descriptors that were found to have the highest resolution from all the different pairs are shown in table VI.

Table VI.

Descriptors that showed the highest resolution for the pairwise separation of artificial signals of bulk fracture and crystal impact from the cubic (undoped) form of KBr, and the dendritic (4080-8120 ppm Pb) form of KBr.

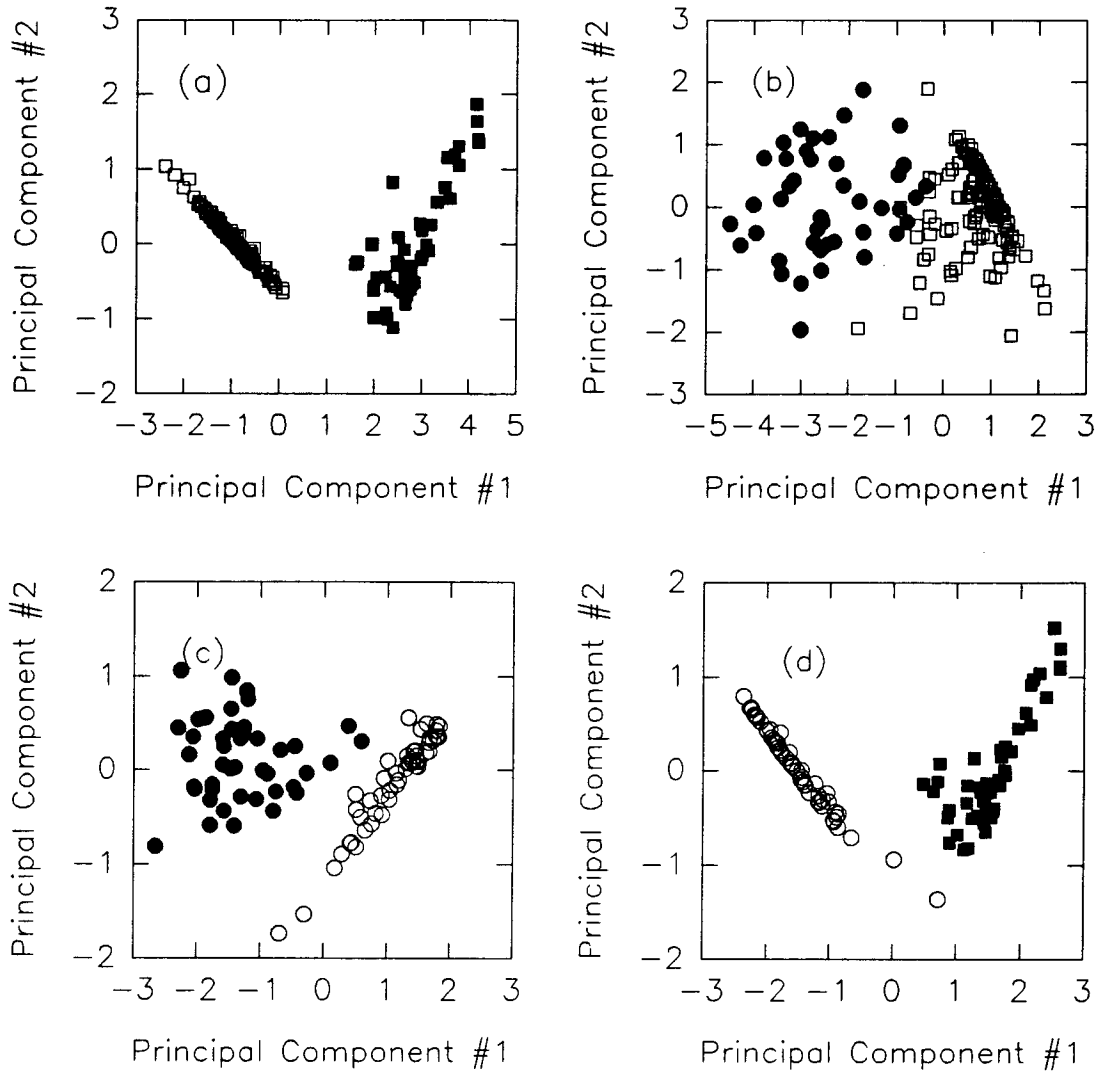
Descriptor Name	
RMS	Root mean square voltage
25-CROSS	Number of times signal crosses $\pm 25\%$ of maximum voltage
10-CROSS	Number of times signal crosses $\pm 10\%$ of maximum voltage
0-CROSS	Number of times signal crosses 0 volts
5/8T	Normalized time octile of root mean square voltage 0.205-0.256 ms
8/8 T	Normalized time octile of root mean square voltage 0.359-0.410 ms
FRQMEAN	Frequency equal to the summation of the intensity-weighted frequencies divided by the total intensity
FRQMED	Frequency at the mid-area of the integrated frequency intensities
DFB1	Normalized for area power spectrum octile 0-156 kHz
DFB4	Normalized for area power spectrum octile 625-781 kHz

The PCA plots in fig. 27, clearly show the ease of separation of the KBr impact signals from the acoustic signals collected during the growth of both morphologies of KBr (fig. 27a, 27d). Note that the separation obtained is much cleaner than might have been expected from fig. 26 alone. The KBr impact signals were also readily separated from the KBr dendrite fracture signals (fig. 28b). The signals obtained from artificially produced

KBr dendrite fracture could be easily distinguished from the KBr crystal growth signals for 0 ppm Pb dopant (fig. 27c) but less easily from the KBr crystal growth signals for 7620 and 5900 ppm Pb dopant (fig. 27b). The KBr crystal growth signals of the two different morphologies could not be distinguished (fig. 28a).

Signals from the six different morphologies of KBr crystal growth (excluding the bulk fracture and impact signals) were also collected using a bandwidth of 2.5 MHz. The subsequent PCA (fig. 29) did not show any increased separation of these classes when compared with the analysis conducted using signals collected with a bandwidth of 1.25 MHz (fig. 26). This lack of separation between the individual classes of signals collected during the crystal growth of different KBr morphologies shows that the two stages of acoustic emission, the first that parallels the image whitening and the second observed after the crystals have visually stopped growing, could not be distinguished by their acoustic signatures using the present descriptors.

This analysis demonstrates that the signals collected during the growth of the dendritic form of KBr (fig. 14b) were more similar to the artificially produced fracture signals than the impact signals. This lends further support to the *inter-crystal interaction* mechanism which involves the inter-microcrystal fracture as the mechanism for acoustic signal generation. This analysis also suggests that the signals which arise during crystal growth might be readily discerned from bulk fracture signals (due to secondary nucleation) and signals from impact of crystals onto a sensor or waveguide that would occur in an industrial crystallizer [53].

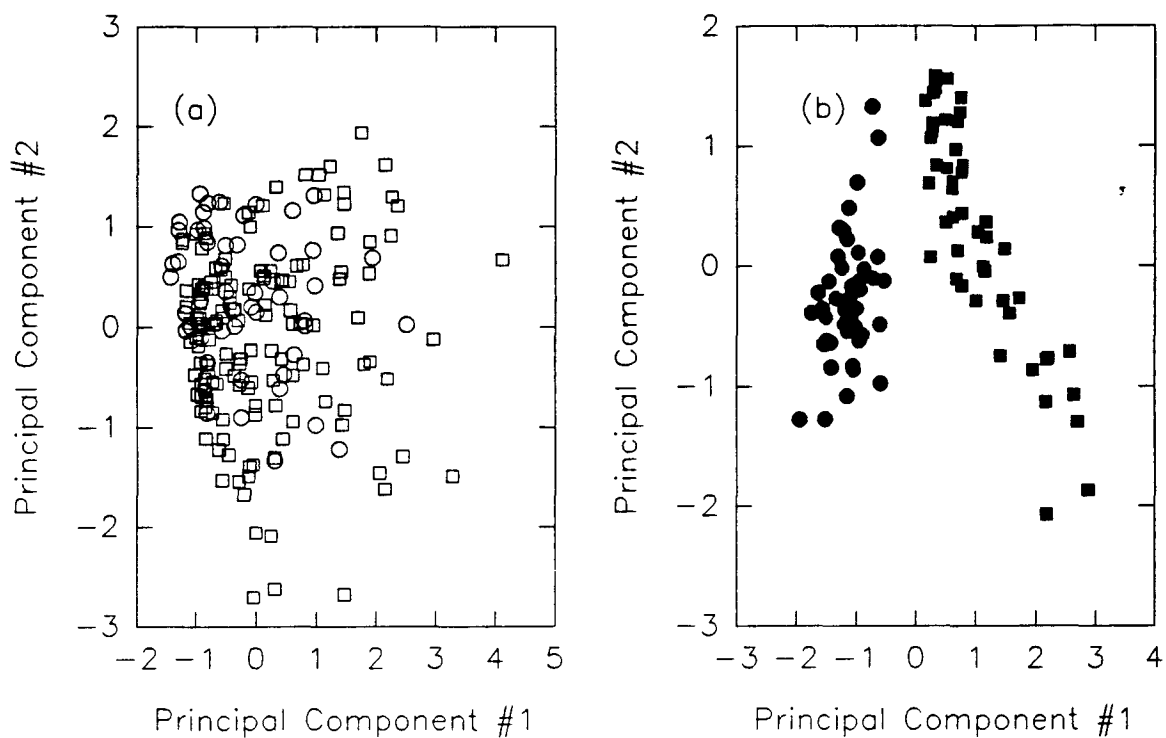


Key:—

Artificially produced signals: KBr crystal growth signals with:

- KBr dendrite fracture ○ 0 ppm Pb dopant
- KBr Impact □ 7620 and 5900 ppm Pb dopant

Fig 27. Principal components analysis showing the separation of acoustic signals that occurred during crystal growth from artificially generated signals mimicking secondary nucleation processes. Descriptors used for separations were (a) RMS, 0-Cross, Frqmean, (b) RMS, 25-Cross, Frqmed, (c) RMS, 10-Cross, 8/8T, (d) RMS, 0-Cross, DFB1 (see table VI).

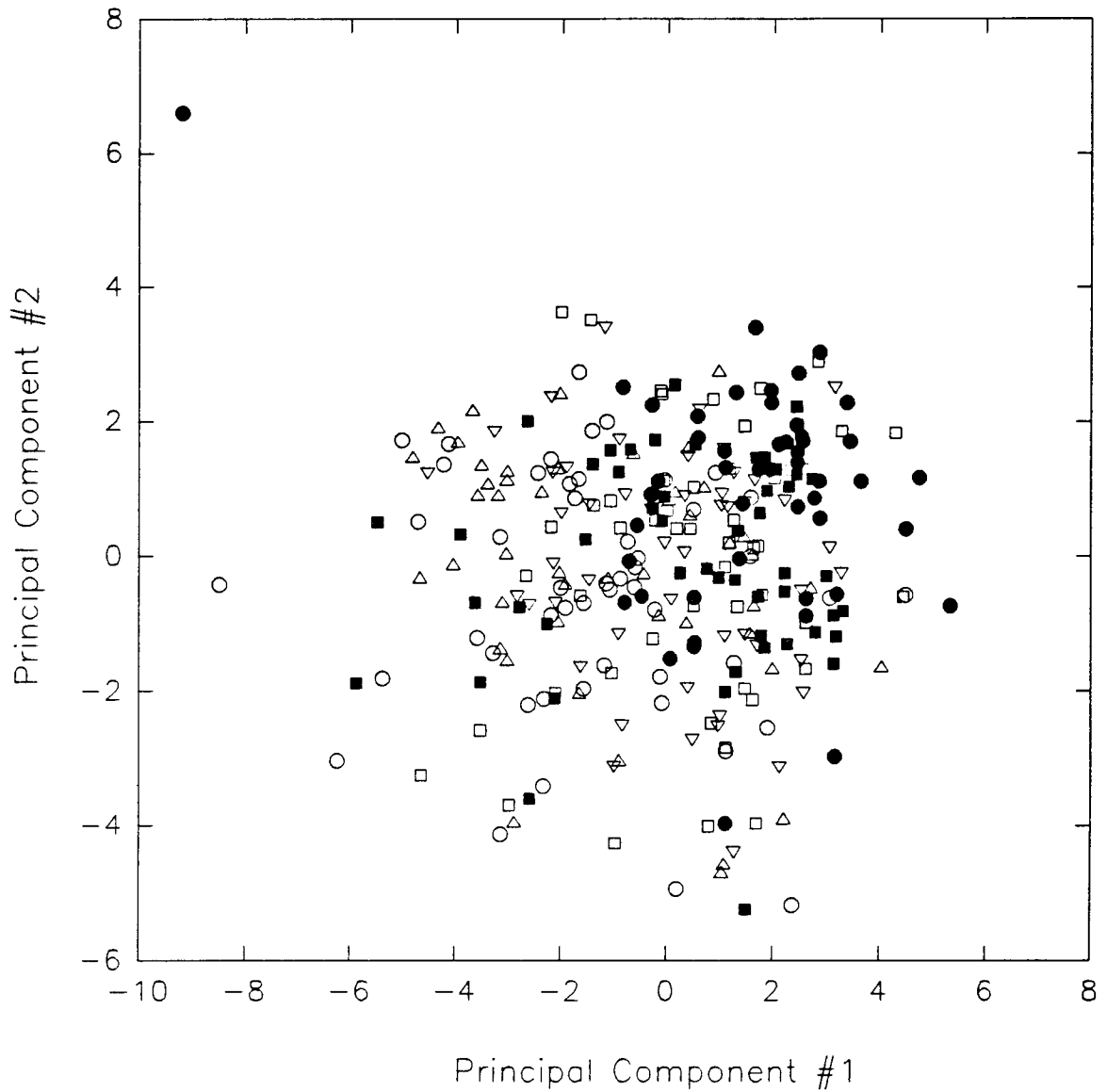


Key:—

Artificially produced signals: KBr crystal growth signals with:

- KBr dendrite fracture ○ 0 ppm Pb dopant
- KBr impact □ 7620 and 5900 ppm Pb dopant

Fig 28. Principal components analysis of acoustic signals collected from both artificially produced crystallization processes, and actual growth processes of different KBr crystal morphologies. Descriptors used for separations were (a) 10-Cross, 5/8T, DFB4, and (b) RMS, 5/8T, 10-Cross (see table VI).



Key:—

KBr crystal growth signals with:

- | | |
|---------------------------|-----------------------|
| ● 0ppm Pb dopant | ○ 15980 ppm Pb dopant |
| □ 3980 ppm Pb dopant | △ 24920 ppm Pb dopant |
| ■ With 7620 ppm Pb dopant | ▽ 29790 ppm Pb dopant |

Fig 29. Principal components analysis of acoustic signals collected with a 2.5 MHz bandwidth during the growth of different KBr crystal morphologies. Only 18 of 32 descriptors were used (see table V).

3.5 Classic Dendritic Growth

The acoustic activity of the dendritic form of KBr observed with 4080-8120 ppm Pb dopant was compared with the classic dendritic growth produced upon evaporation of NH_4Cl . A typical integrated acoustic emission trace observed during the dendritic growth of NH_4Cl is shown in fig. 30. Compare this very stepped curve with the smooth curve observed during the growth of the dendritic form of KBr (figs. 17a, 17b). The total emission observed for the dendritic growth of NH_4Cl is negligible compared with that observed during the growth of the dendritic form of KBr.

These observations were in agreement with predictions based on the nature of the two growth forms. The dendritic growth of NH_4Cl involves the growth of single crystal stems oriented in particular directions (see fig. 3 on p. 15), i.e. no inter-crystal interaction is expected. The source of emissions observed during the growth of this form of NH_4Cl is attributed to the occasional bulk fracture of these stems, an event that does not mimic the growth rate of this form. The resulting stepped curve is indicative of the infrequent fractures of these stems or dislocation movements within the stem. Each step is from a discrete event, whereas the smooth curve observed for the dendritic form of KBr is indicative of many sources of acoustic emission resulting from the interaction of the tiny microcrystals that make up the structure. Obviously, with a small enough time interval between each data point the smooth AE profile observed for the dendritic form of KBr would also show discrete events.

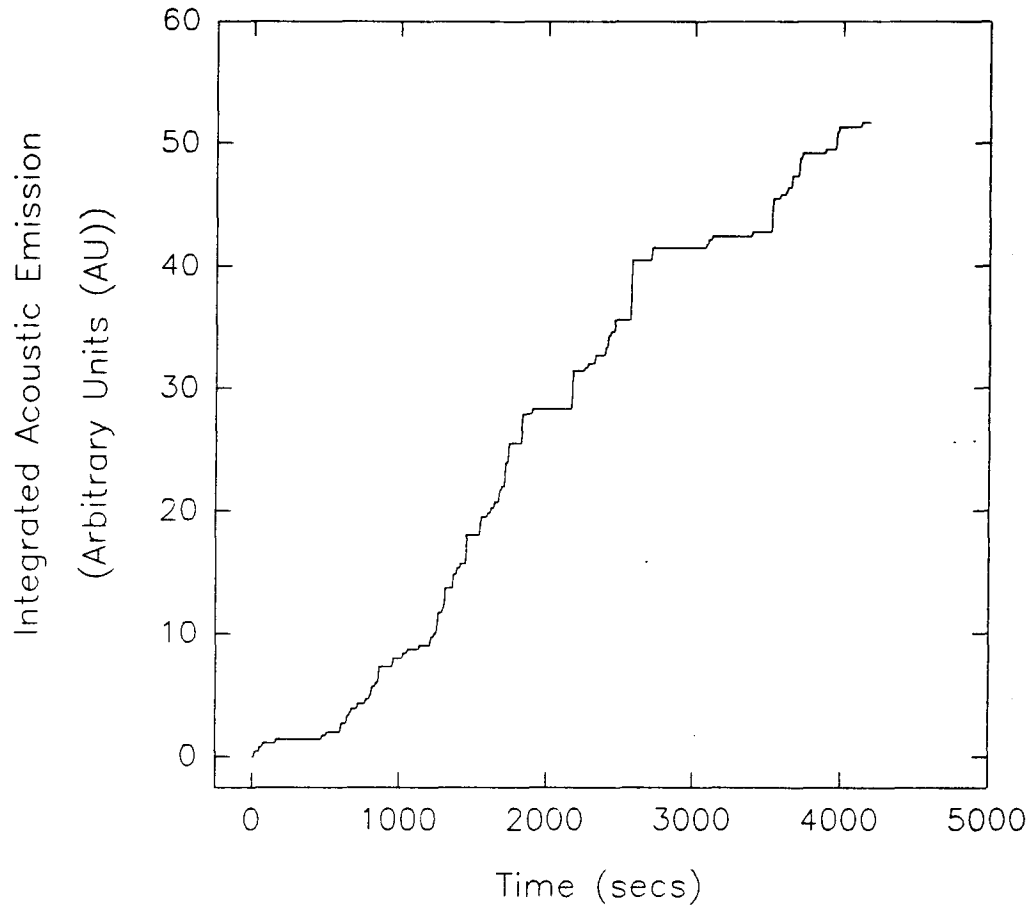


Fig 30. Integrated acoustic emission profile for the dendritic growth of ammonium chloride, showing the infrequent signals, leading to a stepped plot.

Literature Cited

- (1) J. Berlan and T. J. Mason, Ultrasonics, **30(4)**, (1992), 203-212.
- (2) M. A. Bukhnii, L. A. Chernosatonskii and R. G. Maev, J. Microsc., **160(3)**, (1990), 299-313.
- (3) E. T. Zellers, R. M. White and S. M. Rappaport, Anal. Chem., **62**, (1990), 1222-1227.
- (4) H. Coufal and J. F. McClelland, J. Molec. Struct., **173**, (1988), 129-140.
- (5) K. Marr and K. S. Peters, Biochemistry, **30**, (1991), 1254-1258.
- (6) T. Sawada, Y. Gohshi, C. Abe and K. Furuya, Anal. Chem., **57**, (1985), 1743-1745.
- (7) S. D. Lubetkin, J. Appl. Electrochem., **19**, (1989) 668-676.
- (8) P. D. Wentzell, S. J. Vanslyke and K. P. Bateman, Anal. Chim. Acta, **246**, (1991), 43-53.
- (9) E. L. Lube and A. T. Zlatkin, J. Crystal Growth, **98**, (1989), 817-826.
- (10) R. M. Belchamber, D. Betteridge, M. P. Collins, T. Lilley, C. Z. Marczewski and A. P. Wade, Anal. Chem., **58(8)**, (1986), 1873-1877.
- (11) J. A. Simmons and H. N. G. Wadley, J. Research (NIST), **89(1)**, (1984), 55-64.
- (12) O. Lee, Y. Koga and A. P. Wade, Talanta, **37(9)**, (1990), 861-873.
- (13) P. D. Wentzell and A. P. Wade, Anal. Chem., **61**, (1989), 2638-2642.
- (14) A. G. Beattie, J. Acoustic Emission, **2(1-2)**, (1983), 67.
- (15) P. A. Gaydecki, F. M. Burdekin, W. Damaj, D. G. Johns and P. A. Payne, Meas. Sci. Technol., **3**, (1992), 126-134.
- (16) Y. Higo and H. Inaba, J. Acoustic Emission, **8(1/2)**, (1989), 7-24.
- (17) P. D. Wentzell, O. Lee and A. P. Wade, J. Chemom., **5**, (1991), 389-403.
- (18) R. G. Brereton, "Chemometrics: Applications of Mathematics and Statistics to Laboratory Systems", Ellis Horwood Ltd., Chichester, U.K., (1990).

3.6 Primary Nucleation

On tapping the graduated cylinder when the temperature had reached 68°C (2°C of undercooling) a few hexahedral crystals were observed within the solution. After a short period of time (<3 mins) the production of a large number "avalanche" of tiny KBr whiskers was observed in the cylinder. The crystals produced fell through the solution to produce a layer 1-2 cm deep.

The mass primary nucleation observed in the solution produced no detectable acoustic signals. This is in keeping with the crystallization sequences observed for KBr with Pb dopant where the nucleation of individual hexahedral crystals produced no accompanying acoustic emission. The difficulty in separating the onset of acoustic emission from the nucleation of KBr crystals at higher levels of Pb dopant is due purely to the initial clustering of the tiny micro-crystals. The resulting acoustic emission is produced by the inter-crystal interaction mechanism. The whiskers of KBr observed were so small that even their impact on the bottom of the graduated cylinder was not acoustically detectable with the apparatus used. However, this was a function of the attenuation produced by the experimental arrangement

IV CONCLUSIONS

The combination of in-situ optical imaging with acoustic emission and ex-situ morphological analysis has led to the first clear understanding of the mechanism of acoustic signal generation during crystallization. It has been proven that the growth of crystal structures in which many microcrystals are in intimate contact can be followed reliably using acoustic emission. The dendritic form of KBr (4080-8020 ppm Pb dopant) and the octahedral crystal mat (> 12000 ppm Pb dopant) are two such forms. The reproducibility of acoustic emission and optical measurements was surprisingly good, especially when one considers that only a small mass of crystals (0.004-0.12g) was grown.

The importance of determining the exact mechanism of acoustic signal generation during crystallization processes cannot be stressed enough; at present there are no models for these processes. To within the detection limits of our apparatus the growth of a single octahedral microcrystal was not acoustically emissive. However, in all cases interaction of microcrystals during the formation of larger crystal structures produced much emission. For example the dendritic form of KBr fingers that was found to consist of chains of many tiny coupled octahedra produced copious amounts of emission during growth.

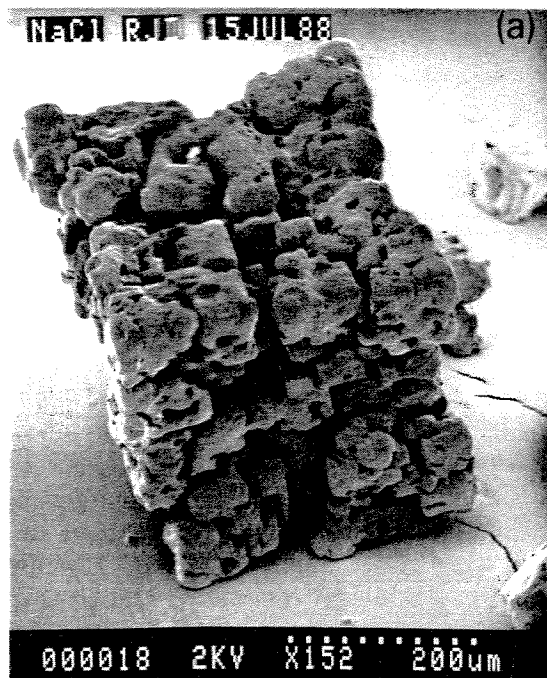
The *inter-crystal interaction mechanism* postulated in this thesis explains all of the observations not only at the microscopic level for the dendritic form of KBr but also at the macroscopic level for the cubic form of KBr, when the initially discrete crystals begin to touch and interact. However it is the interactions of microcrystals during the formation of the dendritic morphology and octahedral mat that make acoustic emission particularly valuable for monitoring the growth of these larger structures.

Primary nucleation of crystals was not detected acoustically during growth of the different KBr morphologies. Indeed even the massive primary nucleation of KBr whiskers was not detectable. From this one may conclude that the onset of crystallization cannot be detected acoustically for these crystal forms. Completion of growth of the dendritic forms of KBr was accompanied by cessation of the observed acoustic emission. For structures where the *inter-crystal interaction* mechanism is the primary source of acoustic signal generation, acoustic emission monitoring is shown to provide a method of following the progress and determining the end of crystal growth.

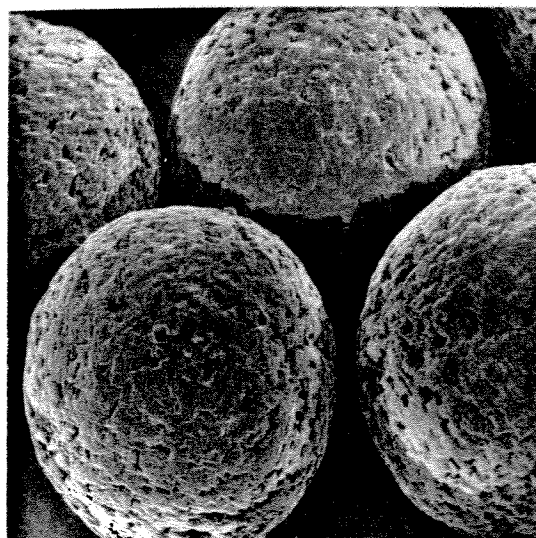
The acoustic signals generated by growth of these KBr morphologies were characteristic of the process and could be readily distinguished from acoustic signals generated by artificially produced dendrite fracture and impact of KBr crystals on the transducer surface. This study provides the basis for the non-invasive monitoring of crystallization whereby acoustic detectors may be used to follow the growth and the processes of secondary nucleation within a solution. The ability to distinguish between signals arising during growth, those produced by impact of crystals suspended in solution, and those produced during bulk fracture will be enhanced if the mechanisms of acoustic generation are known. During this study it was proved possible to separate these different signal classes using *a priori* knowledge. However, the use of acoustic emission for following crystallization processes will only reach its maximum potential when these signals can be unambiguously classified on a routine basis.

V FURTHER WORK

The dendritic form of KBr that produced the most interesting results in this study is a morphology of KBr that occurs when the crystals are grown from solution by evaporation. Industry however uses undercooling (at several degrees below the equilibrium saturation temperature) as the method to produce supersaturated solutions for crystallization. Further work should focus on other dendritic forms of crystals that would be produced in solution. One such system is the growth of sodium chloride doped with sodium ferrocyanide [68]. The dendritic form of NaCl consists of tiny cubelets clustered together to form a larger hexahedral structure (fig. 31a). This is much like the dendritic form of KBr, although the outward appearance of the structure is more ordered. The greater order of this structure may decrease the number of *inter-crystal interactions* and thus lessen the effectiveness of AE for monitoring of this form. A granular form of NaCl can also be produced that appears to consist of a single crystal central core with a polycrystalline outer layer of tiny cubelets arranged to produce a sphere (fig. 31b). This second form might provide more sites for AE due to the less ordered nature of the structure. The study of the NaCl system should provide further insight into the mechanism of acoustic signal generation during crystal growth.



(a)



(b)

Fig 31. Scanning electron micrographs of, (a) dendritic NaCl, (b) granular NaCl. Reproduced from reference [68].

- (19) R. E. Aries, D. P. Lidiard and R. A. Spragg, Chem. Brit., **27(9)**, (1991), 821-824.
- (20) J. W. Mullin, "Crystallisation", Butterworth & Co. Ltd., London, U.K., (1972), p. 136.
- (21) V. A. Garten and R. B. Head, Phil. Mag., **8**, (1963), 1793-1803.
- (22) V. A. Garten and R. B. Head, Phil. Mag., **14(132)**, (1966), 1243-1253.
- (23) N. F. Oputshchennikov, Sov. Phys.-Crystallography, **7(2)**, (1962), 237-239.
- (24) D. P. Lal, R. E. Mason and R. F. Strickland-Constable, J. Crystal Growth, **5**, (1968), 1-8.
- (25) A. N. Chernov, N. P. Zaitseva and L. N. Rashkovich, J. Crystal Growth, **102**, (1990), 793-800.
- (26) R. F. Strickland-Constable, "Kinetics and Mechanism of Crystallization", Academic Press, U.K., (1968), p. 281.
- (27) J. W. Mullin, "Crystallisation", Butterworth & Co. Ltd., London, U.K., (1972), p.170.
- (28) *idem, ibid*, p.196.
- (29) E. G. Cooke, Krist. Tech., **1**, (1966), 119.
- (30) P. R. Collins and W. J. Fredericks, J. Crystal Growth, **71**, (1985), 739-743.
- (31) S. N. Black, R. J. Davey and M. Halcrow, J. Crystal Growth, **79**, (1986), 765-774.
- (32) R. J. Davey, J. Crystal Growth, **76**, (1986), 637-644.
- (33) J. R. Bourne and R. J. Davey, J. Crystal Growth, **44**, (1978), 613-614.
- (34) H. Svanoë, Chem. Eng. Prog., **55(5)**, (1959), 47-54.
- (35) L. Phoenix, Brit. Chem. Eng., **11(1)**, (1966), 34-38.
- (36) F. Grases and J. G. March, TrAC, Trends in Analytical Chem., **10(6)**, (1991), 190-195.
- (37) J. W. Mullin and A. Amatavivadhana, J. Appl. Chem., **17**, (1967), 151-156.

- (38) R. J. Davey, R. I. Ristic and B. Zizic, **J. Crystal Growth**, **47**, (1979), 1-4.
- (39) R. C. Mattel and R. S. Feigelson, **J. Crystal Growth**, **97**, (1989), 333-336.
- (40) B. Liang and R. W. Hartel, **J. Crystal Growth**, **108**, (1991), 129-142.
- (41) G. A. Hussman, K. A. Berglund and M. A. Larson, **Appl. Spec.**, **39(3)**, 1985, 560-562.
- (42) H. Takubo and H. Makita, **J. Crystal Growth**, **94**, (1989), 469-474.
- (43) J. H. Bilgram and R. Steininger, **J. Crystal Growth**, **99**, (1990), 30-37.
- (44) D. Cunningham, R. J. Davey, K. J. Roberts, J. N. Sherwood and T. Shripathi, **J. Crystal Growth**, **99**, (1990), 1065-1069.
- (45) W. M. Zuk and K. B. Ward, **J. Crystal Growth**, **110**, (1991), 148-155.
- (46) S. Kozelak, D. Martin, J. Ng and A. McPherson, **J. Crystal Growth**, **110**, (1991), 177-181.
- (47) W. M. Rosenblum, J. P. Kennedy and B. Bishop, **J. Crystal Growth**, **110**, (1991), 171-176.
- (48) D.L. Portgal and E. Burstein, **Phys. Rev.**, **170(3)**, (1968), 673-678.
- (49) A. S. Pine, **Phys. Rev. B**, **2(6)**, (1970), 2049-2054.
- (50) C. Lin, F. Tao, Z. Shen and W. Ma, **Phys. Rev. Lett.**, **58(20)**, (1987), 2095-2098.
- (51) D. Betteridge, M. T. Joslin and T. Lilley, **Anal. Chem.**, **53**, (1981), 1064-1073.
- (52) B. F. Munro, M.Sc. Thesis, University of British Columbia, (1991).
- (53) J. G. Bouchard, M. J. Beesley and J. A. Salkfeld, 3rd International Symposium on Analytical Techniques for Process Control, Atlanta, April 1992, Abstract L59.
- (54) A. Galeski, L. Koenczoel, E. Piorkowska and E. Baer, **Nature**, **325**, (1987), 40-41.
- (55) A. Galeski, L. Koenczoel, E. Piorkowska and E. Baer, **J. Polymer Sci. Part B**, **28**, (1990), 1171-1186.

- (56) J. Shen, D. Xu, R. Yao, R. Liu and D. Li, Chin. J. Polymer Sci., **8(1)**, (1990), 69-74.
- (57) O. Hunderi and K. Lønvik, Proc. 3rd Int. Conf. "Rapidly Quenched Metals", Brighton, U.K., 3-7th July 1978, B. Cantor (ed.), Volume 1, pp. 375-82, Met. Soc.: London, U.K., July 1978.
- (58) J. G. Delly, Micro-Notes, **6(1)**, 1979.
- (59) J. E. Huheey, Inorganic Chemistry, 3rd edn., Harper and Row, New York, p. 56.
- (60) I. Tarjan and M. Matrai (eds.), "Laboratory Manual on Crystal Growth", Akademiai Kiado, Budapest, (1972), pp. 44-58.
- (61) B. P. Agarwal, Indian. J. Phys., **56A**, (1982), 312-322.
- (62) G. W. Sears, J. Chem. Phys., **29(5)**, (1958), 1045-1048.
- (63) P. D. Wentzell, S. J. Vanslyke and A. P. Wade, TrAC, Trends in Analytical Chem., **9(1)**, (1990), 3-8.
- (64) A. A. Pollock, J. Acoustic Emission, **9(2)**, 1990, 140-141.
- (65) I. H. Brock, O. Lee, K. A. Soulsbury, P. D. Wentzell, D. Sibbald and A. P. Wade, Chemom. Intell. Lab. Sys., **12**, (1992), 271-290.
- (66) H. L. Keller, J. Less Comm. Met., **109**, (1985), 19-29.
- (67) K. A. Soulsbury, A. P. Wade and D. Sibbald, Chemom. Intell. Lab. Sys., **15**, (1992), 87.
- (68) R. J. Davey, M. M. Harding and R. J. Rule, J. Crystal Growth, **114**, (1991), 7-12.